







PTP-MEG2 regulates quantal size and fusion pore opening through two distinct structural bases and substrates

Yun-Fei Xu^{1,2,*†} , Xu Chen^{3,†} , Zhao Yang¹, Peng Xiao¹, Chun-Hua Liu⁴, Kang-Shuai Li^{1,2}, Xiao-Zhen Yang⁵, Yi-Jing Wang¹, Zhong-Liang Zhu⁶, Zhi-Gang Xu⁷, Sheng Zhang⁸, Chuan Wang⁹, You-Chen Song¹⁰, Wei-Dong Zhao¹¹ , Chang-He Wang¹², Zhi-Liang Ji⁵, Zhong-Yin Zhang⁸, Min Cui^{3,**} , Jin-Peng Sun^{1,***}  & Xiao Yu^{3,****} 

Abstract

Tyrosine phosphorylation of secretion machinery proteins is a crucial regulatory mechanism for exocytosis. However, the participation of protein tyrosine phosphatases (PTPs) in different exocytosis stages has not been defined. Here we demonstrate that PTP-MEG2 controls multiple steps of catecholamine secretion. Biochemical and crystallographic analyses reveal key residues that govern the interaction between PTP-MEG2 and its substrate, a peptide containing the phosphorylated NSF-pY⁸³ site, specify PTP-MEG2 substrate selectivity, and modulate the fusion of catecholamine-containing vesicles. Unexpectedly, delineation of PTP-MEG2 mutants along with the NSF binding interface reveals that PTP-MEG2 controls the fusion pore opening through NSF independent mechanisms. Utilizing bioinformatics search and biochemical and electrochemical screening approaches, we uncover that PTP-MEG2 regulates the opening and extension of the fusion pore by dephosphorylating the DYNAMIN2-pY¹²⁵ and MUNC18-1-pY¹⁴⁵ sites. Further structural and biochemical analyses confirmed the interaction of PTP-MEG2 with MUNC18-1-pY¹⁴⁵ or DYNAMIN2-pY¹²⁵ through a distinct structural basis compared with that of the NSF-pY⁸³ site. Our studies thus provide mechanistic insights in complex exocytosis processes.

Keywords catecholamine; exocytosis; PTP-MEG2; structure; tyrosine phosphorylation

Subject Categories Membrane & Trafficking; Post-translational Modifications & Proteolysis; Structural Biology

DOI 10.15252/embr.202052141 | Received 20 November 2020 | Revised 26 January 2021 | Accepted 18 February 2021 | Published online 25 March 2021

EMBO Reports (2021) 22: e52141

Introduction

Secretion via vesicle exocytosis is a fundamental biological event involved in almost all physiological processes (Wu *et al*, 2014; Neher & Brose, 2018; Dittman & Ryan, 2019). The contents of secreted vesicles include neuronal transmitters, immune factors, and other hormones (Alvarez de Toledo *et al*, 1993; Sudhof, 2013; Magadmi *et al*, 2019). There are three major exocytosis pathways in secretory cells, namely, full-collapse fusion, kiss-and-run, and compound exocytosis, which possess different secretion rates and release amount (Sudhof, 2004). It has previously been reported that the phosphorylation of critical proteins at serine/threonine or tyrosine residues participates in stimulus–secretion coupling in certain

- 1 Key Laboratory Experimental Teratology of the Ministry of Education and Department of Biochemistry and Molecular Biology, Shandong University School of Medicine, Jinan, China
 - 2 Department of General Surgery, Qilu Hospital of Shandong University, Jinan, China
 - 3 Key Laboratory Experimental Teratology of the Ministry of Education and Department of Physiology, Shandong University School of Medicine, Jinan, China
 - 4 Department of Physiology, Shandong First Medical University, Taian, China
 - 5 State Key Laboratory of Cellular Stress Biology, School of Life Sciences, Xiamen University, Xiamen, China
 - 6 School of Life Sciences, University of Science and Technology of China, Hefei, China
 - 7 Shandong Provincial Key Laboratory of Animal Cells and Developmental Biology, School of Life Sciences, Shandong University, Jinan, China
 - 8 Departments of Medicinal Chemistry and Molecular Pharmacology and of Chemistry, Center for Cancer Research, and Institute for Drug Discovery, Purdue University, West Lafayette, IN, USA
 - 9 Department of Pharmacology, Hebei Medical University, Shijiazhuang, China
 - 10 Department of Medical Biophysics, University of Toronto, Toronto, ON, Canada
 - 11 Department of Developmental Cell Biology, China Medical University, Shenyang, China
 - 12 Center for Mitochondrial Biology and Medicine, The Key Laboratory of Biomedical Information Engineering of Ministry of Education, School of Life Science and Technology, Xi'an Jiaotong University, Xi'an, China
- *Corresponding author. Tel: +86 15064111921; E-mail: xuyunfei1988@126.com
 **Corresponding author. Tel: +88382571; E-mail: cuimin@sdu.edu.cn
 ***Corresponding author. Tel: +88382346; E-mail: sunjinpeng@sdu.edu.cn
 ****Corresponding author (lead contact). Tel: +88381910; E-mail: yuxiao@sdu.edu.cn
 †These authors contributed equally to this work

important exocytosis processes, for example, the secretion of insulin from pancreatic β cells and the secretion of catecholamine from the adrenal medulla (Seino *et al*, 2009; Ortsater *et al*, 2014; Laidlaw *et al*, 2017). However, the exact roles of protein tyrosine phosphatases (PTPs) in the regulation of key hormone secretion procedures are not fully understood.

The 68-kDa PTP-MEG2, encoded by *ptpn9*, is a non-receptor classical PTP encompassing a unique N-terminal domain with homology to the human CRAL/TRIO domain and yeast Sec14p (Gu *et al*, 1992; Alonso *et al*, 2004; Huynh *et al*, 2004; Cho *et al*, 2006; Zhang *et al*, 2012; Zhang *et al*, 2016). The N-terminal Sec14p homology domain of PTP-MEG2 recognizes specific phospholipids in the membrane structure and is responsible for its specific subcellular location. In secretory immune cells, PTP-MEG2 has been suggested to regulate vesicle fusion via direct dephosphorylation of the pY⁸³ site of N-ethylmaleimide-sensitive fusion protein (NSF; Huynh *et al*, 2004). However, many key issues regarding PTP-MEG2-regulated cell secretion remain controversial or even unexplored. For example, it is uncertain whether PTP-MEG2 regulates vesicle exocytosis only within immune cells (Zhang *et al*, 2016) and only plays insignificant roles in other hormone secretion processes. It remains elusive whether PTP-MEG2 regulates vesicle trafficking pathways other than the NSF-mediated vesicle fusion.

Functional characterization of PTP-MEG2 *in vivo* normally requires a knockout model; however, PTP-MEG2-deficient mice show neural tube and vascular defects, and the lack of PTP-MEG2 is embryonic lethal (Wang *et al*, 2005). Alternatively, a specific small-molecule inhibitor of PTP-MEG2 has fast response with no compensatory effects, enabling it to serve as a powerful tool to investigate PTP-MEG2 functions (Zhang *et al*, 2012; Yu & Zhang, 2018). Recently, we have developed a potent and selective PTP-MEG2 inhibitor, Compound 7, that has a K_i of 34 nM and shows at least 10-fold selectivity for PTP-MEG2 over more than 20 other PTPs (Zhang *et al*, 2012). The application of this selective PTP-MEG2 inhibitor in combination with electrochemical approaches enabled us to reveal that PTP-MEG2 regulates multiple steps of catecholamine secretion from the adrenal medulla by controlling the vesicle size, the release probabilities of individual vesicles, and the initial opening of the fusion pore during exocytosis. Further crystallographic studies of the PTP-MEG2 protein in complex with the pY⁸³-NSF fragment and enzymological kinetic studies captured the transient interaction between PTP-MEG2 and NSF and provided the structural basis for PTP-MEG2 substrate specificity. Interestingly, by delineating the substrate specificity of deficient PTP-MEG2 mutants in the study of catecholamine secretion from primary chromaffin cells, our results suggested that PTP-MEG2 regulates the initial opening of the fusion pore during exocytosis by regulating substrates other than the known NSF through a distinct structural basis. We therefore took advantage of this key knowledge and utilized bioinformatics analysis, GST pull-down screening, and enzymological and electrochemical techniques to identify the potential key PTP-MEG2 substrates involved in fusion pore opening. These experiments led to the identification of several new PTP-MEG2 substrates in the adrenal medulla, of which DYNAMIN2-pY¹²⁵ and Mammalian homolog of Unc-18 (MUNC18)-1-pY¹⁴⁵ are the crucial dephosphorylation sites of PTP-MEG2 in the regulation of initial pore opening and expansion. Further crystallographic analyses and functional assays with MUNC18-1 Y¹⁴⁵ and DYNAMIN2-pY¹²⁵ revealed the mechanism

underlying the recognition of MUNC18-1 and DYNAMIN2 by PTP-MEG2 and how these PTP-MEG2-mediated dephosphorylation events regulate fusion pore dynamics.

Results

Phosphatase activity of PTP-MEG2 is required for catecholamine secretion from adrenal glands

Endogenous PTP-MEG2 expression was readily detected in mouse adrenal gland and chromaffin cell line PC12 cells (Appendix Fig S1A and B). Because PTP-MEG2 knockout is embryonic lethal (Wang *et al*, 2005), we applied our newly developed active site-directed and active site-specific PTP-MEG2 inhibitor (Compound 7) to investigate the functional roles of PTP-MEG2 in catecholamine secretion from adrenal glands (Appendix Fig S1C). Compound 7 is a potent and cell-permeable PTP-MEG2 inhibitor, with a K_i value of 34 nM and extraordinary selectivity against other phosphatases (Zhang *et al*, 2012). The administration of either high concentrations of potassium chloride (70 mM) or 100 nM angiotensin II (AngII) significantly increased the secretion of both epinephrine (EPI) and norepinephrine (NE) from the adrenal medulla as previously reported (Teschemacher & Seward, 2000; Liu *et al*, 2017), and this effect was specifically blocked by pre-incubation with Compound 7 (400 nM) for 1 h (Fig 1A–D). Notably, basal catecholamine secretion also decreased after pre-incubation with Compound 7 (Fig 1A–D). However, the intracellular catecholamine contents did not change in response to Compound 7 incubation (Appendix Fig S1D and E). These results indicate that PTP-MEG2 plays an essential role in catecholamine secretion from the adrenal medulla.

PTP-MEG2 inhibition reduces the quantal size and the release probabilities of catecholamine secretion from individual vesicles

We used the carbon fiber electrode (CFE) to characterize the effects of PTP-MEG2 inhibition on the kinetics of catecholamine secretion from primary cultured chromaffin cells (Chen *et al*, 2005; Harada *et al*, 2015; Fig 1E and F, Appendix Fig S1F and G). The Ang II-induced catecholamine secretion was gradually attenuated by increasing the concentration of Compound 7 after pre-incubation with the primary chromaffin cells, from 20% at 100 nM Compound 7 to 80% at 2 μ M Compound 7 (Fig 1E and F, Appendix Fig S1F–H). We then compared individual amperometric spikes of chromaffin cells pre-incubated with different concentrations of Compound 7 to determine the effect of PTP-MEG2 inhibition on quantal size (total amperometric spike charge) and vesicle release probabilities. The application of PTP-MEG2 inhibitor reduced quantal size, as indicated by statistical analysis of the quantal size distribution and averaged amperometric spike amplitude (Fig 1G and Appendix Fig S1I). Specifically, the peak of the amperometric spikes decreased from 1.1 pC to 0.5 pC after incubation with 400 nM Compound 7 (Fig 1G). The number of AngII-induced amperometric spikes also significantly decreased in the presence of Compound 7 (Appendix Fig S1J).

We then used transmission electron microscopy to examine the location of the large-dense-core vesicles (LDCVs) in the adrenal medulla after incubation with AngII and Compound 7 (Fig 1H and I,

Appendix Fig S2A and B). The intracellular distribution of the LDCVs was summarized by 50 nm bins according to their distance from the chromaffin plasma membrane (Fig 1J). Vesicles with distance less than 50nm were generally considered to be in the docking stage. Here we found that the application of 400 nM Compound 7 significantly decreased the number of docking vesicles in contact with the plasma membrane (Fig 1J). Moreover, Compound 7 significantly increased the number of LDCVs with a

diameter less than 50 nm and decreased the number of LDCVs with a diameter > 150 nm (Fig 1K), consistent with the statistical analysis of the total amperometric spike charge obtained by electrochemical measurements (Appendix Fig S1H–M). This change of vesicle size in the adrenal medulla was in accordance with the functional studies of PTP-MEG2 in immunocytes, which identified that vesicles were excessively larger if PTP-MEG2 was overexpressed (Huynh et al, 2004).

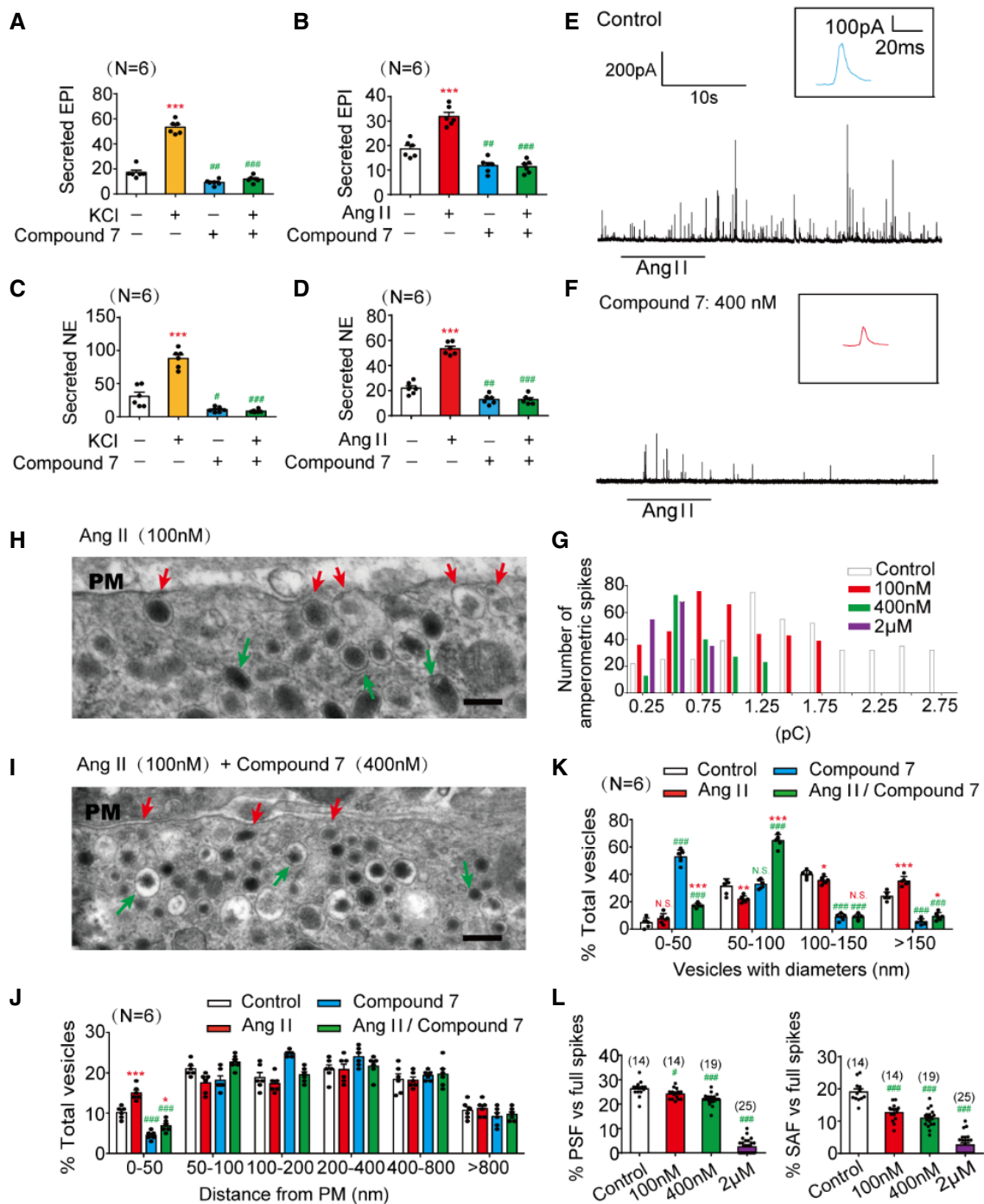


Figure 1.

Figure 1. Inhibition of PTP-MEG2 reduced the spike amplitude and “foot” probability of catecholamine secretion.

- A–D The epinephrine (A, B) or norepinephrine (C, D) secreted from the adrenal medulla was measured by ELISA method after stimulation with high KCl (70 mM) (A, C) or angiotensin II (AngII, 100 nM) (B, D) for 1 min, with or without pre-incubation with a specific PTP-MEG2 inhibitor (400 nM) for 1 h.
- E, F Amperometric spikes of primary mouse chromaffin cells induced by AngII (100 nM) were determined by electrochemical experiments after incubation with PTP-MEG2 inhibitor at different concentrations.
- G The distribution of the quantal size of AngII (100 nM)-induced amperometric spikes by primary chromaffin cells after incubation with different concentrations of PTP-MEG2 inhibitor. Histograms show the number of amperometric spikes of different quantal sizes.
- H, I Secretory vesicles of primary chromaffin cells were examined by transmission electron microscopy after 100 nM AngII stimulation, with or without pre-incubation with 400 nM Compound 7. Scale bars: (H, I), 150 nm. Red arrows indicate morphologically docked LDCVs, and green arrows stand for undocked LDCVs. PM represents plasma membrane.
- J Vesicle numbers according to different distances from the plasma membrane were calculated in the presence or absence of 100 nM AngII or 400 nM Compound 7. PM represents plasma membrane.
- K The percentage of vesicles with different diameters was measured after 100 nM AngII stimulation or incubation with 400 nM Compound 7. Compound 7 significantly decreased vesicle size under AngII stimulation.
- L The percentage of pre-spike foot (PSF) (left panel) and stand-alone foot (SAF) (right panel) was calculated after incubation with the indicated concentrations of Compound 7.

Data information: Data were analyzed using one-way ANOVA and displayed as the mean \pm s.e.m. (A–D, J–L) * P < 0.05; ** P < 0.01; *** P < 0.001: cells stimulated with KCl or AngII compared with un-stimulated cells. # P < 0.05; ## P < 0.01; ### P < 0.001: cells pre-incubated with PTP-MEG2 inhibitors compared with control vehicles. N.S. means no significant difference. Data were from 6 (A–D, J–K) or 8 (L) independent experiments. # indicates P < 0.05 and ### indicates P < 0.001 compared with control group.

PTP-MEG2 regulates the initial opening of the fusion pore

Generally, the presence of pre-spike foot (PSF) is a common phenomenon preceding large amperometric spikes which indicate catecholamine secretion in chromaffin cells, while stand-alone foot (SAF) is considered to represent “kiss-and-run” exocytosis (Chen *et al*, 2005). Both PSF and SAF are usually considered as indications of the initial opening of the fusion pore (Alvarez de Toledo *et al*, 1993; Zhou *et al*, 1996). In the present study, Compound 7 substantially decreased the PSF frequency from 25 to 3% and attenuated the SAF frequency from 18 to 4% in response to AngII stimulation (Fig 1L). Consistent with PSF/SAF frequency, the inhibitor Compound 7 also decreased the average duration, amplitude, and charge (Appendix Fig S2C–J).

The crystal structure of the PTP-MEG2/phospho-NSF complex reveals significant structural rearrangements in the WPD loop and β 3-loop- β 4

PTP-MEG2 is known to modulate interleukin-2 secretion in macrophages via dephosphorylation of NSF, a key regulator in vesicle fusion (Huynh *et al*, 2004). In response to stimulation with either high potassium chloride or AngII, the two stimulators for catecholamine secretion from the adrenal medulla, the tyrosine phosphorylation of NSF increased, indicating that NSF phosphorylation actively participates in catecholamine secretion (Fig 2A, Appendix Fig S3A and B). Moreover, a significant portion of NSF co-localized with PTP-MEG2 in the adrenal medulla upon AngII stimulation, and the substrate-trapping mutant PTP-MEG2-D⁴⁷⁰A

Figure 2. Interaction of PTP-MEG2 and tyrosine-phosphorylated NSF in the medulla and the crystal structure of the PTP-MEG2/phospho-NSF-segment complex.

- A NSF was phosphorylated after stimulation with AngII or KCl. Adrenal medulla cells were stimulated with 100 nM AngII or 70 mM KCl for 5 min and lysed. NSF was immunoprecipitated with a specific NSF antibody coated with Protein A/G beads. A pan-phospho-tyrosine antibody pY²⁰ was used in Western blot to detect the tyrosine-phosphorylated NSF in the adrenal medulla under different conditions.
- B NSF was co-localized with PTP-MEG2 in the adrenal medulla. After stimulation with 100 nM AngII, NSF and PTP-MEG2 in the adrenal medulla were visualized with immunofluorescence. White arrow stands for co-localization of the PTP-MEG2 and NSF.
- C Analysis of PTP-MEG2 and NSF fluorescence intensities by Pearson's correlation analysis. Pearson's correlation coefficient was 0.7.
- D Phosphorylated NSF interacted with PTP-MEG2. PC12 cells were transfected with FLAG-NSF. After stimulation of the cells with 100nM AngII in the presence or absence of 100 μ M H₂O₂ for 5 min (H₂O₂ was exploited to increase the overall tyrosine phosphorylation of the cellular proteins), the potential PTP-MEG2 substrate in cell lysates was pulled down with GST-PTP-MEG2-D⁴⁷⁰A or GST control.
- E The overall structure of PTP-MEG2-C⁵¹⁵A/D⁴⁷⁰A in complex with the NSF-pY⁸³ phospho-segment.
- F The 2Fo-Fc annealing omit map (contoured at 1.0 σ) around the NSF-pY⁸³ phospho-segment. The P-loop was highlighted in blue.
- G Plot of distance RMSDs of individual residues between the crystal structures of the PTP-MEG2/NSF-pY⁸³ phospho-peptide complex (PDB: 6KZQ) and the PTP-MEG2 native protein (PDB: 2PA5).
- H Superposition of the PTP-MEG2/NSF-pY⁸³ phospho-peptide complex structure (red) on the PTP-MEG2 native protein structure (PDB: 2PA5, blue). The structural rearrangement of the WPD loop and β 3-loop- β 4 is highlighted.
- I, J The closure of the WPD loop and corresponding conformational changes in the inactive state (I) and the active state (J) of PTP-MEG2. The rotation of R⁵²¹ leads to the movement of W⁴⁶⁸ and a corresponding 7 Å movement of the WPD loop.
- K, L The structural rearrangement of β 3-loop- β 4 of PTP-MEG2 in the active state (L) compared with the inactive state (K). The disruption of the salt bridge between E⁴⁰⁶ and R⁵²¹ contributed to the new conformational state of the N-terminal of β 3-loop- β 4.
- M, N The conformational change of the P-loop of the inactive state (M) and the active state of PTP-MEG2 in response to NSF-pY⁸³ segment binding (N). The disruption of the charge interaction between R⁴⁰⁹ and D³³⁵ resulted in the movement of the main chain from G⁴⁰⁸ to K⁴¹¹.

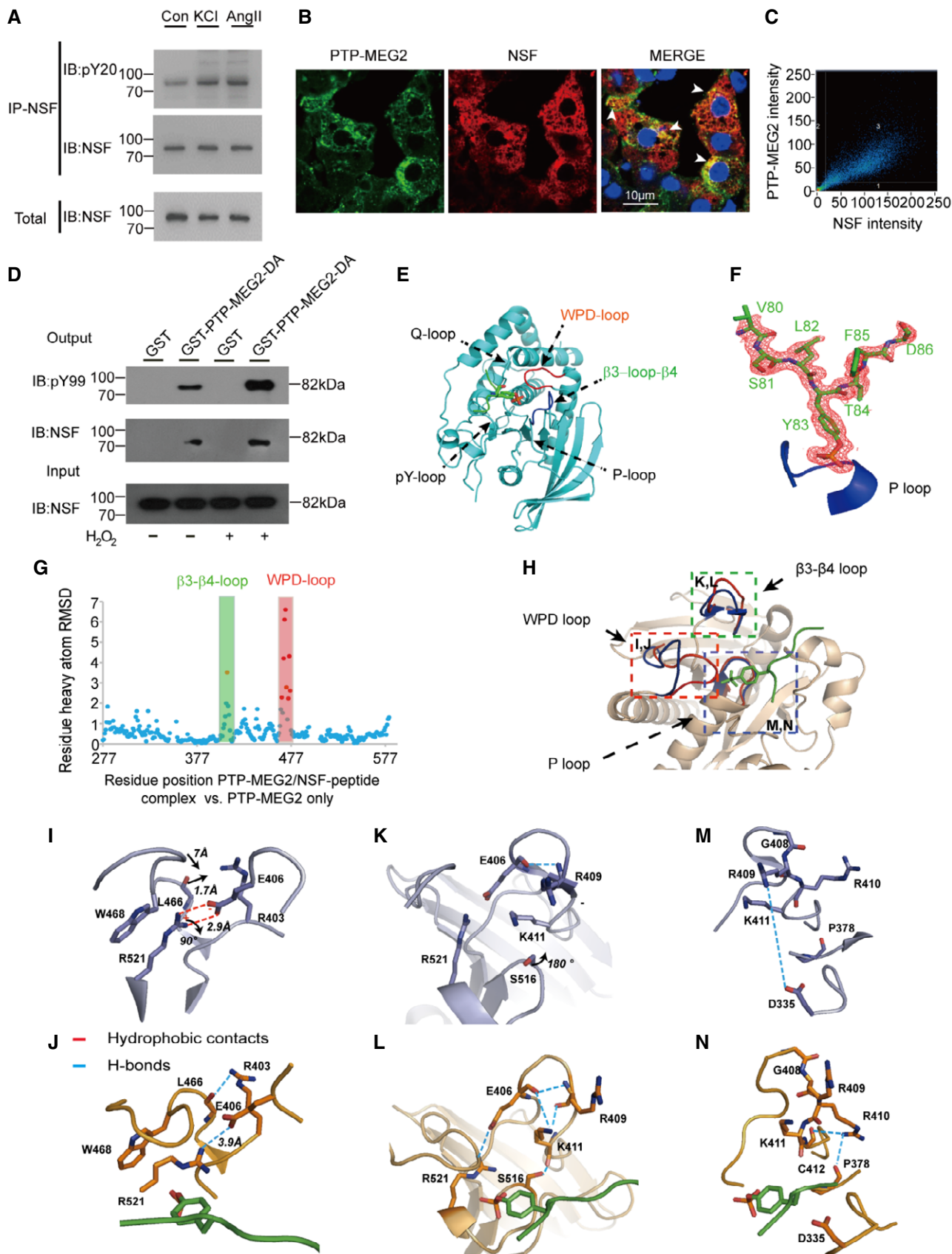


Figure 2.

interacted with the tyrosine-phosphorylated NSF from the adrenal medulla treated with hydrogen peroxide (Fig 2B–D, Appendix Fig S3C–E), suggesting that PTP-MEG2 regulates catecholamine secretion in chromaffin cells through direct dephosphorylation of NSF. Hydrogen peroxide was used to elevate the overall protein tyrosine phosphorylation levels in cells because it is permeable to cell and can oxidize the catalytic cysteine located in the active site of the PTP catalytic domains (Kanda *et al*, 2006; Frijhoff *et al*, 2014).

We therefore co-crystallized PTP-MEG2/phospho-NSF-E⁷⁹-pY⁸³-K⁸⁷, and the structure was solved at 1.7 Å resolution (Table 1). The 2Fo-Fc electron density map allowed for the unambiguous assignment of the phospho-NSF-E⁷⁹-pY⁸³-K⁸⁷ in the crystal structure (Fig 2E

and F). Importantly, the binding of phospho-NSF-E⁷⁹-pY⁸³-K⁸⁷ induced substantial conformational changes in both the WPD loop and β3-loop-β4 compared to the crystal structure of PTP-MEG2 alone (Barr *et al*, 2009; Fig 2G and H). Specifically, the interaction of the phosphate group of pY⁸³ of NSF with the guanine group of R⁵²¹ of PTP-MEG2 induced rotation of approximately 90 degrees, which resulted in the movement of W⁴⁶⁸ and a traverse of 7 Å of the WPD loop for a closed state (Fig 2I and J). Unique to the PTP-MEG2/substrate complex, the movement of L⁴⁶⁶ in the WPD loop by 1.7 Å enabled the formation of a new hydrogen bond between its main chain carbonyl group and the side chain of R⁴⁰³ (Fig 2I and J). The disruption of the salt bridge between E⁴⁰⁶ and R⁵²¹ also contributed to the new conformational state of the N-terminal of the β3-loop-β4 (Fig 2K and L). The presence of the phosphate in the PTP-MEG2 active site C-terminal to β3-loop-β4 caused a 180-degree rotation of the side chain of S⁵¹⁶, allowing its side chain oxygen to form a new hydrogen bond with the main chain carbonyl of group K⁴¹¹ (Fig 2K and L). This structural rearrangement altered the side chain conformation of K⁴¹¹, which pointed to the solvent region and formed new polar interactions with E⁴⁰⁶ and the carbonyl group of R⁴⁰⁹ (Fig 2K and L). Moreover, the presence of the phospho-NSF-E⁷⁹-pY⁸³-K⁸⁷ peptide between R⁴⁰⁹ and D³³⁵ disrupted their charge interactions, enabling a movement of the main chain from G⁴⁰⁸ to K⁴¹¹, accompanied by a side chain movement of R⁴¹⁰ and the formation of new polar interactions with the main chain of P³⁷⁸ and C⁴¹² (Fig 2M and N). These structural rearrangements that occurred in the WPD loop and β3-loop-β4 enabled the accommodation of the phospho-substrate of PTP-MEG2 and may be important for its appropriate interactions with its physiological substrates/partners and subsequent activation.

Table 1. Crystallographic data and refinement statistics.

Data collection	PTP-MEG2. NSF pY ⁸³ peptide	PTP-MEG2. MUNC18-1 pY ¹⁴⁵ peptide
Space group	p2 ₁ 2 ₁ 2	p2 ₁ 2 ₁ 2
Cell dimensions		
a (Å)	71.447	71.048
b (Å)	83.708	84.074
c (Å)	48.615	48.753
α (deg)	90	90
β (deg)	90	90
γ (deg)	90	90
Resolution (Å)	80–1.70 (1.76–1.70) ^a	54.3–2.08 (2.08–2.20) ^a
Unique observations	32,748 (3167) ^a	18,019 (1773) ^a
Completeness (%)	99.6 (98.3) ^a	99.8 (99.8) ^a
Redundancy	3.8 (3.8) ^a	6.1 (6.3) ^a
<I>/<σ>	22.22 (2.34) ^a	6.5 (2.3) ^a
R _{merge}	0.064 (0.477) ^a	0.191 (0.927) ^a
Structure refinement	80–1.70	
Resolution (Å)	1.70	2.08
Reflections used for R _{work} /R _{free}	31,212/1536	17,995/896
R _{work} /R _{free} ^b (%)	0.1900/0.2173	0.2102/0.2304
Average B-factor		
Protein	20.98	35.36
Peptide	31.525	53.25
RMSD ideal bonds (Å)	0.008	0.008
RMSD ideal angles (deg)	1.212	0.968
Ramachandran plot (%)		
Most favored	93.73	93.56
Allowed	4.88	6.10
Generously allowed	1.39	0.34
Disallowed	0	0

The values in parentheses correspond to the highest resolution shell.

^aEach dataset was collected from a single crystal.

Structural basis of the PTP-MEG2-NSF interaction

The structural analysis identified critical residues for the phospho-substrate recognition by PTP-MEG2 (Fig 3A). PTP-MEG2 Y³³³ forms extensive hydrophobic interactions with the phenyl ring of pY⁸³ in NSF. Mutation of this residue caused a significant decrease of more than 8-fold in activity for both p-nitrophenyl phosphate (pNPP) and the phospho-NSF-peptide (Fig 3B and C), suggesting that this residue is important for PTP-MEG2 recognition of all substrates with phenyl rings. N-terminal to pY⁸³, the side chain oxygen of S⁸¹ formed a hydrogen bond with the carbonyl oxygen of the main chain of R³³² of PTP-MEG2. The carbonyl oxygen of the main chain of S⁸¹ formed a hydrogen bond with the amide group of G³³⁴, and L⁸² formed hydrophobic interactions with the side chain of D³³⁵ (Fig 3A). Specifically, mutation of G³³⁴ to R impaired the activity of PTP-MEG2 toward the NSF-pY⁸³ phospho-peptide but did not affect on its intrinsic phosphatase activity as measured by using pNPP as a substrate, suggesting that G³³⁴ plays an important role in the recognition of the N-terminal conformation of the peptide substrate (Fig 3B and C, Appendix Table S1).

The D³³⁵ in the pY binding loop of PTP-MEG2 is also critical for determining the peptide orientation of the substrate by forming important hydrogen bonds with the main chain amide and carbonyl groups of pY⁸³ and T⁸⁴ in NSF. Residues C-terminal to NSF-pY⁸³, T⁸⁴, and F⁸⁵ formed substantial hydrophobic interactions with V³³⁶, F⁵⁵⁶, Q⁵⁵⁹, and Y⁴⁷¹ (Fig 3A). Accordingly, mutation of D³³⁵A or Q⁵⁵⁹A showed no significant effect on pNPP activity but substantially decreased their activities toward the phospho-NSF peptide (Fig 3B

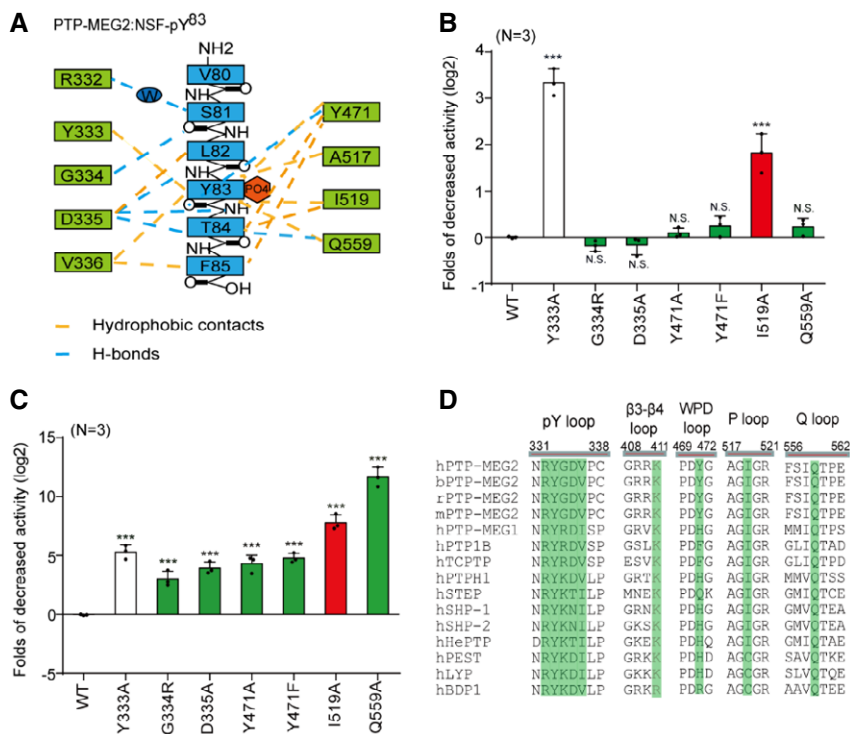


Figure 3. Molecular determinants of PTP-MEG2 interaction with the NSF-pY⁸³ site.

A Schematic representation of interactions between PTP-MEG2 and the NSF-pY⁸³ site.
B Relative values of the decreased phosphatase activities of different PTP-MEG2 mutants toward pNPP (p-Nitrophenyl phosphate) compared with wild-type PTP-MEG2.
C Fold change decreases in the phosphatase activities of different PTP-MEG2 mutants toward the NSF-pY⁸³ phospho-segment compared with wild-type PTP-MEG2.
D Sequence alignment of PTP-MEG2 from different species and with other PTP members. Important structural motifs participating in phosphatase catalysis or the recognition of the NSF-pY⁸³ site are shown, and key residues contributing to the substrate specificity are highlighted.

Data information: *** $P < 0.001$; PTP-MEG2 mutants compared with the control group. Data were obtained from 3 independent experiments. N.S. means no significant difference. All the data were analyzed using one-way ANOVA and displayed as the mean \pm s.e.m. In (B, C), the red column indicates that the mutation sites have greater effects on the enzyme activities toward phospho-NSF segment than the pNPP. The green column indicates that the mutation sites only have significant effects on the enzyme activity toward NSF phospho-segment but not pNPP. The white column stands for the mutants that have similar effects on pNPP and NSF phospho-segment.

and C, Appendix Table S1). Mutation of I⁵¹⁹A caused a decrease in the intrinsic activity of PTP-MEG2 and a further decrease of approximately 256-fold in its ability to dephosphorylate phospho-NSF-peptide. Moreover, Y⁴⁷¹ formed extensive hydrophobic interactions with T⁸⁴ and F⁸⁵ and a hydrogen bond with the carboxyl group of pY⁸³. Mutation of Y⁴⁷¹ to either A or F greatly reduced its activity toward the phospho-NSF-E⁷⁹-pY⁸³-K⁸⁷ peptide but had little effects on pNPP dephosphorylation. Taken together, the structural analyses and enzymological studies identified G³³⁴, D³³⁵, Y⁴⁷¹, I⁵¹⁹, and Q⁵⁵⁹ as critical residues for the substrate recognition of NSF by PTP-MEG2. Importantly, although none of these residues are unique to PTP-MEG2, the combination of these residues is not identical across the PTP superfamily but is conserved in PTP-MEG2 across different species, highlighting the important roles of these residues in mediating specific PTP-MEG2 functions (Fig 3D, Appendix Fig S4).

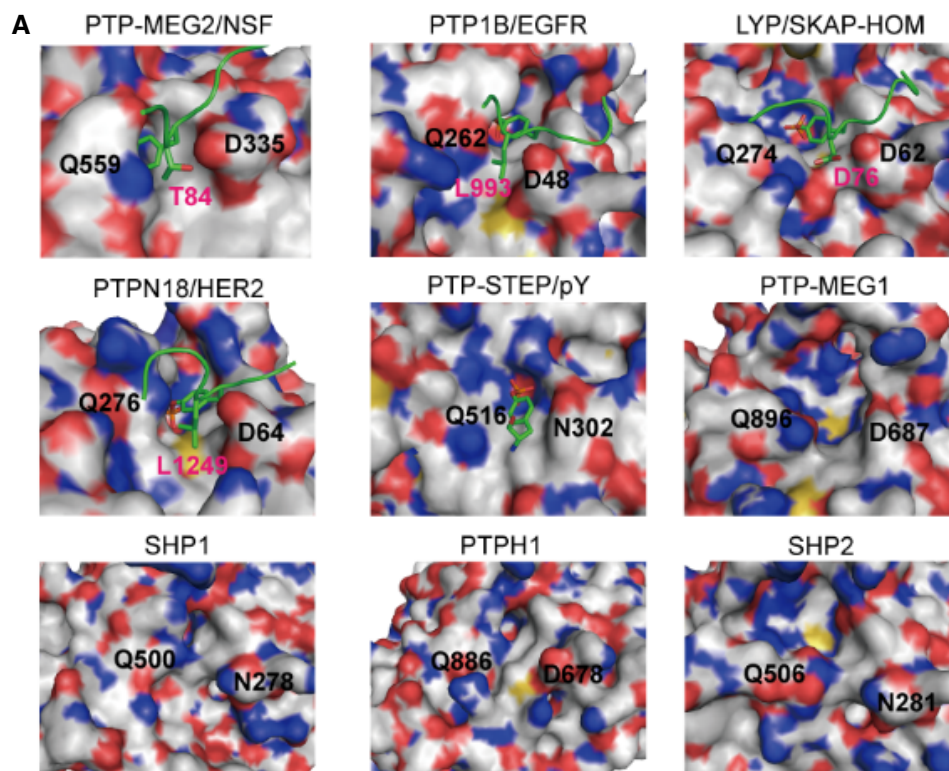
Molecular determinants of Q⁵⁵⁹:D³³⁵ for the substrate specificity of PTP-MEG2

The pY + 1 pocket is an important determinant of substrate specificity in different PTP superfamily members (Barr *et al*, 2009; Yu *et al*, 2011; Wang *et al*, 2014; Li *et al*, 2016). The pY + 1 pocket of

PTP-MEG2 was found to consist of D³³⁵, V³³⁶, F⁵⁵⁶, and Q⁵⁵⁹ (Fig 4A). Unique to the PTP-MEG2/NSF-E⁷⁹-pY⁸³-K⁸⁷ complex structure, a relatively small T⁸⁴ residue occurred at the pY + 1 position, in contrast to L⁹⁹³ in the PTP1B/EGFR-pY⁹⁹² complex structure, D⁷⁶ in the lymphoid-specific tyrosine phosphatase (LYP)/ Src kinase-associated protein of 55 kDa homolog (SKAP-HOM)-pY⁷⁵ complex structure, and L¹²⁴⁹ in the PTPN18/ human receptor tyrosine-protein kinase erbB-2 (HER2)-pY¹²⁴⁸ complex structure (Fig 4A). Although several PTPs have an equivalent D: Q pair similar to D³³⁵:Q⁵⁵⁹ of PTP-MEG2 determining the entrance of the pY + 1 residue into the pY + 1 pocket, such as PTP1B, LYP, PTPN18, Striatum-enriched protein tyrosine phosphatase (STEP), PTP-MEG1, SHP1, PTPH1, and SHP2, structural analysis indicated that the Cβ between Q⁵⁵⁹ and D³³⁵ is the smallest in PTP-MEG2, at least 1 Å narrower than the other PTP structures examined (Fig 4B). The narrower pY + 1 pocket entrance could be a unique feature for substrate recognition by PTP-MEG2.

PTP-MEG2 regulates two different steps of catecholamine secretion through dephosphorylation of different substrates

We then infected primary chromaffin cells with lentivirus encoding wild-type PTP-MEG2 or different mutants for electrochemical



B

Complex	PDB code	pY+1	Distance(C β)	
PTP-MEG2/NSF(pY83)		T	10.42	D335:Q559
PTP1B/EGFR(pY992)	1EEN	L	11.46	D48:Q262
LYP/SKAP-HOM(pY75)	3OMH	D	11.32	D63:Q274
PTPN18/HER2(pY1248)	4GFU	L	11.89	D64:Q276
PTP-STEP/pY	2CJZ		12.43	N312:Q516
PTP-MEG1	2I75		11.16	D687:Q896
SHP1	4HJQ		12.27	N278:Q500
PTPH1	4QUN		12.35	D678:Q886
SHP2	3B7O		12.44	N281:Q506

Figure 4. The tip opening of the pY + 1 pocket is critical for PTP-MEG2 substrate specificity.

A Surface representations of the complex structures of PTP-MEG2-C⁵¹⁵A/D⁴⁷⁰A/NSF-pY⁸³, PTP1B-C²¹⁵A/EGFR-pY⁹⁹² (PDB: 1EEN), LYP-C²²⁷S/SKAP-HOM-pY⁷⁵ (PDB: 3OMH), PTPN18-C²²⁹S/HER2-pY¹²⁴⁸ (PDB: 4GFU), and PTP-STEP/pY (PDB: 2CJZ). Crystal structures of PTP-MEG1 (PDB: 2I75), SHP1 (PDB: 4HJQ), PTPH1 (PDB: 4QUN), and SHP2 (PDB: 3B7O). The pY + 1 sites are highlighted.

B Summary of the distance between the C β atoms of D³³⁵ and Q⁵⁵⁹ (corresponding to PTP-MEG2 number) of the pY + 1 pocket in PTP-MEG2 and other classical non-receptor PTPs bearing the same residues at similar positions.

investigation of the structure–function relationship of PTP-MEG2 in the regulation of catecholamine secretion (Fig 5A, Appendix Figs S5A–G and S6A–D). In addition to the wild-type PTP-MEG2, we chose 6 PTP-MEG2 mutants, including G³³⁴R, D³³⁵A, Y⁴⁷¹A, Y⁴⁷¹F, I⁵¹⁹A, and Q⁵⁵⁹A, whose positions are

determinants of the interactions between PTP-MEG2 and NSF from the pY⁸³-1 position to the pY⁸³+2 position (Fig 5B). Cells with approximately 15-fold of overexpressed exogenous PTP-MEG2 wild type or mutants than the endogenous PTP-MEG2 were selected for electrochemical studies (Appendix Fig S5E and F). The PTP-MEG2

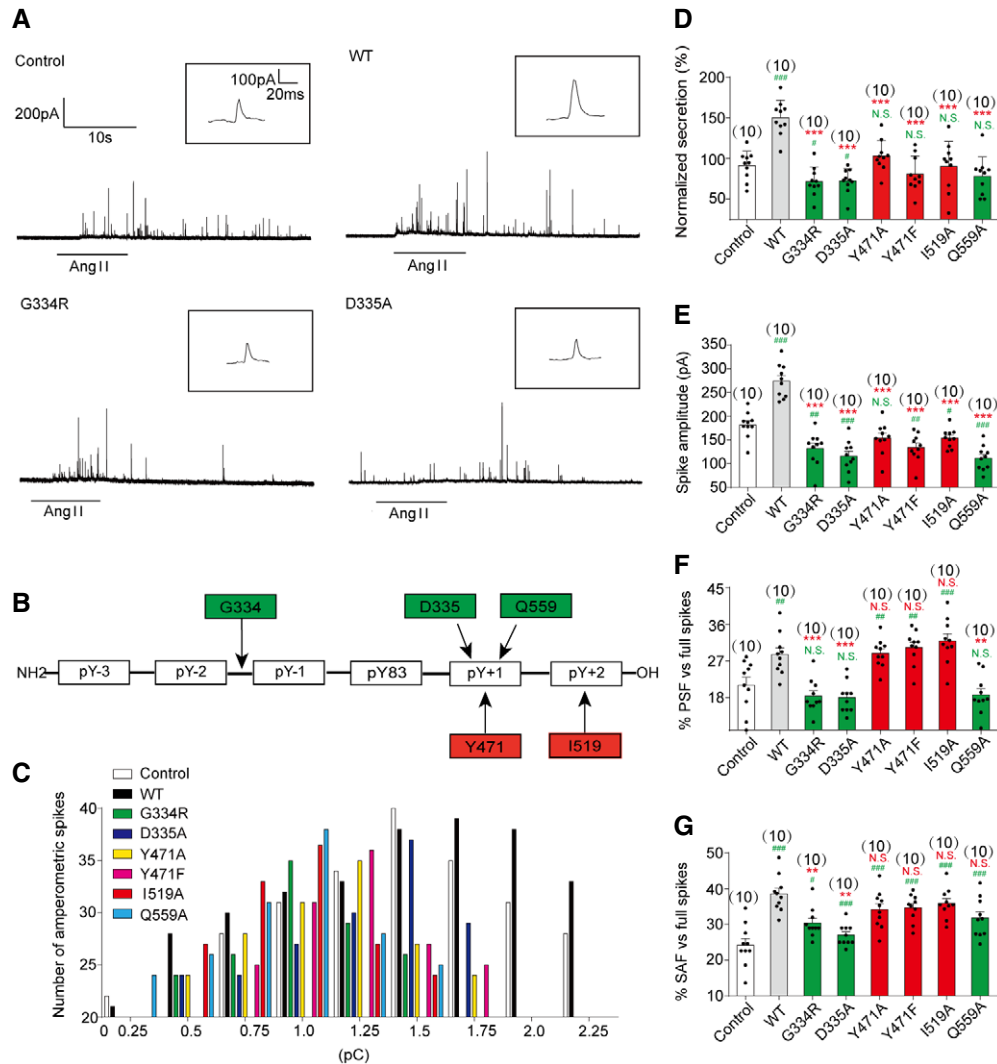


Figure 5. Effects of different PTP-MEG2 mutants on properties of catecholamine secretion from primary chromaffin cells.

- A** Primary mouse chromaffin cells were transduced with a lentivirus containing the gene for wild-type PTP-MEG2 or different mutants with a GFP tag at the C-terminus. Positive transfected cells were confirmed with green fluorescence and selected for electrochemical analysis. Typical amperometric current traces evoked by AngII (100 nM for 10 s) in the control (transduced with control vector) (top left panel), WT (top right panel), G³³⁴R (bottom left panel), and D³³⁵A (bottom right panel) are shown.
- B** The schematic diagram shows key residues of PTP-MEG2 defining the substrate specificity adjacent to the pY⁸³ site of NSF.
- C** The distribution of the quantal size of chromaffin cells transduced with lentivirus containing the genes encoding different PTP-MEG2 mutants.
- D** Statistical diagram of the quantal size in Fig 5A and Appendix Fig S6A–D. The secretion amount of each group was standardized with respect to the control group.
- E–G** Calculated parameters of secretory dynamics, including the spike amplitude (E), PSF frequency (F), and SAF frequency (G).

Data information: (B, D–G) Green color represents the amino acids which are found to modulate foot probability based on structure analysis, and red color means amino acids which does not regulate foot probability. (D–G), * indicates PTP-MEG2 mutant overexpression group compared with the WT overexpression group. # indicates the overexpression group compared with the control group. ** $P < 0.01$; *** $P < 0.001$ and # $P < 0.05$; ## $P < 0.01$; ### $P < 0.001$. N.S. means no significant difference. Data were from six independent experiments. All the data were analyzed using one-way ANOVA and showed as the mean \pm s.e.m.

mutations did not significantly affect its interaction with NSF, suggesting that residues not located within the active site of PTP-MEG2 may also participate in NSF associations (Appendix Figs S5G). The overexpression of wild-type PTP-MEG2 significantly increased both the number and amplitude of the amperometric spikes, which are indicators of the release probabilities of individual vesicles and their quantal sizes, respectively (Fig 5C–E, Appendix Fig S6E). In contrast, the expression of G³³⁴R, D³³⁵A,

Y⁴⁷¹A, Y⁴⁷¹F, I⁵¹⁹A, and Q⁵⁵⁹A all significantly decreased the quantal size, the release probabilities of individual vesicles, the half-width, and the rise rate of each spike (Fig 5C–E, Appendix Fig S6E, F and H). However, there was no difference in the rise time between these mutations and the wild type (Appendix Fig S6G). These results suggest that the interaction of PTP-MEG2 with NSF is important for controlling vesicle size and the release probability of catecholamine secretion.

Unexpectedly, the PTP-MEG2 mutants showed different effects on the probabilities of both PSF and SAF (Fig 5F and G). G³³⁴R mutation which disrupted the recognition of the N-terminal conformation of the peptide substrate of PTP-MEG2, and D³³⁵A and Q⁵⁵⁹A, which are the determinants of pY + 1 substrate specificity, significantly reduced the AngII-induced foot probabilities. The mutations of I⁵¹⁹ and Y⁴⁷¹, which formed specific interactions with T⁸⁴ and F⁸⁵ of NSF and are determinants of the C-terminal region of the central phospho-tyrosine involved in the substrate specificity of PTP-MEG2, showed no significant effects (Fig 5B, F and G, Appendix Fig S6I–N). These results indicate that PTP-MEG2 regulates the initial opening of the fusion pore via a distinct structural basis from that of vesicle fusion, probably through dephosphorylating other unknown substrates. As D³³⁵A and Q⁵⁵⁹A of PTP-MEG2 maintained the occurrence of the foot probability, the unknown PTP-MEG2 substrate that regulates the fusion pore opening should have a small residue, such as G, A, S, or T at the pY + 1 position. Conversely, the unknown PTP-MEG2 substrate should have a less hydrophobic residue at the pY + 2 position because Y⁴⁷¹F, Y⁴⁷¹A, and I⁵¹⁹A of PTP-MEG2 had no significant effects on the foot probability.

Identification of new PTP-MEG2 substrates that contributed to the initial opening of the fusion pore

The effects of PTP-MEG2 mutations along the PTP-MEG2/NSF phospho-segment interface on catecholamine secretion indicated that a PTP-MEG2 substrate other than NSF with distinct sequence characteristics contributes to the regulation of “foot probability” (Fig 5). We therefore utilized this key information to search for new potential PTP-MEG2 substrates by bioinformatics methods (Fig 6A). First, we searched for the keywords “fusion pore”, “secretory vesicle” and “tyrosine phosphorylation” using the functional protein association network STRING and the text mining tool PubTator, which resulted in a candidate list of 51 proteins (Appendix Table S2, Table EV1). Second, we applied UniProt by selecting proteins located only in the membrane or vesicle, which limited the candidates to 28 members (Appendix Table S3). Third, as our experiments were carried out in the adrenal gland, we used the Human Protein Atlas database for filtering to exclude the proteins which is not detectable in adrenal gland, which narrowed the candidate list to 23 proteins. Finally, we

exploited the post-translational-motif database PhosphoSitePlus to screen candidate proteins with potential phospho-sites that matched the sequence requirements at both the pY + 1 position and the pY + 2 position, which are “G, S, A, T, V, P” and “G, A, S, T, C, V, L, P, D, H”, respectively. These positions were further evaluated by surface exposure if a structure was available. The combination of these searches produced 12 candidate lists with predicted pY positions (Fig 6B).

To biochemically characterize whether these proteins are substrates of PTP-MEG2, we transfected the plasmids encoding the cDNAs of these candidate proteins into PC12 cells, stimulated the cells with AngII, and performed a pull-down assay with the GST-PTP-MEG2-D⁴⁷⁰A trapping mutant or GST controls. The known PTP-MEG2 substrate NSF was used as a positive control. Notably, six candidates, including protein kinase C and casein kinase substrate in neurons protein 1 (PACSIN1), MUNC18-1, vesicle-associated membrane protein 7 (VAMP7), synaptosomal-associated protein 25 (SNAP25), DYNAMIN1, and DYNAMIN2, showed specific interactions with PTP-MEG2 after AngII stimulation in PC12 cells (Fig 6C, Appendix Fig S7A and B). Whereas the protein of MUNC18-1, VAMP7, DYNAMIN2, and SNAP25 was readily detected in the adrenal medulla, DYNAMIN1 and PACSIN1 showed substantially lower expression than that in the liver and brain (Appendix Fig S7C). Moreover, whereas MUNC18-1, VAMP7, and DYNAMIN2 strongly co-localized with PTP-MEG2 in the adrenal medulla (Fig 6D–F), the co-localization of SNAP25 and PACSIN1 with PTP-MEG2 was relatively weak (Appendix Fig S7D and E). Therefore, MUNC18-1, VAMP7, and DYNAMIN2 are more likely candidate PTP-MEG2 substrates which were further strengthened by the fact that the high potassium chloride- or AngII-stimulated tyrosine phosphorylation of these proteins in the adrenal medulla was significantly dephosphorylated by PTP-MEG2 *in vitro* (Appendix Fig S8A–C and E), whereas the tyrosine phosphorylation of SNAP25 had no obvious change (Appendix Fig S8D and E).

PTP-MEG2 regulates the initial opening of the fusion pore through dephosphorylating MUNC18-1- pY¹⁴⁵

The predicted PTP-MEG2 dephosphorylation site on MUNC18-1 (also called STXBP1) is Y¹⁴⁵, which localizes on the β sheet linker

Figure 6. Identification of potential candidate substrates of PTP-MEG2 that participate in fusion pore initiation and expansion.

- A Flowchart for the workflow to predict the candidate substrates of PTP-MEG2 during fusion pore initiation and expansion. A total of 51 proteins were enriched with the functional protein association network STRING and the text mining tool PubTator by searching the keywords “fusion pore”, “secretory vesicle” and “tyrosine phosphorylation”. These proteins were filtered with UniProt by selecting proteins located only in the membrane or vesicle, which resulted in 28 candidates. The Human Protein Atlas database was then applied to exclude proteins with no expression in the adrenal gland. Finally, we used the post-translational-motif database PhosphoSitePlus to screen candidate proteins with potential phospho-sites that matched our sequence motif prediction at the pY + 1 or pY + 2 positions.
- B After the bioinformatics analysis, a total of 12 candidate PTP-MEG2 substrates that may participate in fusion pore initiation and expansion and their potential phospho-sites were displayed.
- C The GST pull-down assay suggested that PACSIN1, MUNC18-1, VAMP7, SNAP25, DYNAMIN1, and DYNAMIN2 directly interact with PTP-MEG2. PC12 cells were transfected with plasmids of candidate substrates, including SYN1, MUNC18-3, PACSIN1, SCAMP1, MUNC18-1, PPP3CA, STX17, VAMP7, SYT7, SYT11, SNAP25, DYNAMIN1, and DYNAMIN2 stimulated with 100 nM AngII. The tyrosine phosphorylation of these proteins was verified by specific anti-pY antibodies (Appendix Fig S8A–E). The potential substrates of PTP-MEG2 in cell lysates were pulled down with a GST-PTP-MEG2-D⁴⁷⁰A trapping mutant and then detected by Western blot. White arrow stands for Western blot band consistent with the predicted molecular weight of the potential PTP-MEG2 substrate.
- D–F Co-immunostaining assays of PTP-MEG2 with potential substrates in the adrenal medulla. MUNC18-1, VAMP7, and DYNAMIN2 all showed strong co-localization with PTP-MEG2 after 100 nM AngII stimulation in the adrenal medulla. White arrow stands for co-localization of PTP-MEG2 with MUNC18-1, VAMP7, or DYNAMIN2. Pearson’s correlation coefficients for (D, E, and F) were 0.61, 0.65, and 0.79 respectively. The co-immunostaining results of PTP-MEG2 with other potential substrates are shown in Appendix Fig S7.

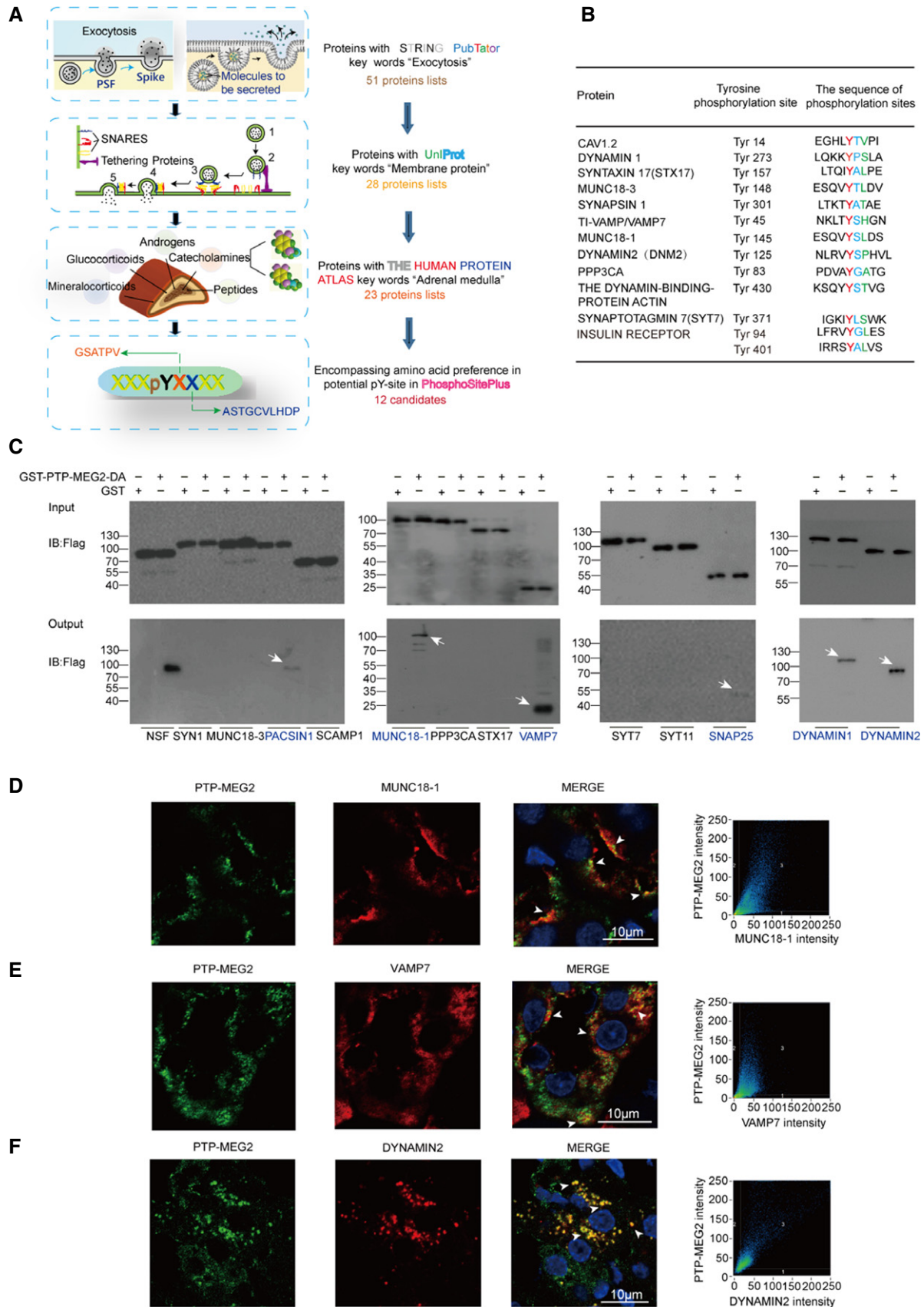


Figure 6.

and forms extensive hydrophobic interactions with surrounding residues (Hu *et al*, 2011; Yang *et al*, 2015; Fig 7A, Appendix Fig S9A). Moreover, the phenolic oxygen of Y¹⁴⁵ forms specific hydrogen bonds with the main chain amide of F⁵⁴⁰ and the main chain carbonyl oxygens of I⁵³⁹ and G⁵⁶⁸ (Fig 7B). These key interactions might be involved in regulating the arrangement of the arc shape of the three domains of MUNC18-1, by tethering the interface between domain 1 and domain 2. The phosphorylation of Y¹⁴⁵ likely abolishes this H-bond network and changes its ability to associate with different snare complexes participating in vesicle fusion procedures (Fig 7B). Interestingly, a missense mutation of MUNC18-1 Y¹⁴⁵H was found to be associated with early infantile epileptic encephalopathy (Stamberger *et al*, 2017; Fig 7C).

Notably, the Y¹⁴⁵H missense mutation may not be phosphorylated properly. We therefore overexpressed wild-type MUNC18-1, Y¹⁴⁵A, a non-phosphorylatable mutant, Y¹⁴⁵E, a phosphomimetic mutant, Y¹⁴⁵F, a non-phosphomimetic mutant, and the disease-related Y¹⁴⁵H mutant in PC12 cells stimulated with AngII and then examined their abilities to interact with PTP-MEG2 trapping mutant. The GST pull-down results indicated that all MUNC18-1 Y¹⁴⁵ mutations significantly decreased their ability to associate with PTP-MEG2 (Fig 7D, Appendix Fig S8G and H). In contrast, mutation of the predicted phosphorylation sites of SNAP25, the SNAP25-Y¹⁰¹A, had no significant effect on their interactions with PTP-MEG2 (Appendix Fig S8F–H). These results suggested that pY¹⁴⁵ is one of the major sites of MUNC18-1 regulated by PTP-MEG2 (Fig 7D).

Next, primary chromaffin cells were infected by the following four types of lentivirus encoding wild-type MUNC18-1, the

MUNC18-1 Y¹⁴⁵-tyrosine phosphorylation-deficient mutant Y¹⁴⁵F, the MUNC18-1 Y¹⁴⁵-tyrosine phosphorylation mimic mutant Y¹⁴⁵E, and the disease-related mutant Y¹⁴⁵H. The Y¹⁴⁵E is a phosphorylation mimic mutant of pY¹⁴⁵, which generate a negative charge at this specific site. In contrast, the Y¹⁴⁵F could not be phosphorylated because of lack of the phenolic oxygen. We examined the effects of these mutants using primary chromaffin cells harboring approximately 20–40-fold MUNC18-1 overexpression related to that of expression level of endogenous wild-type MUNC18-1 (Appendix Fig S9B–D). Interestingly, Y¹⁴⁵E or Y¹⁴⁵H of MUNC18-1 significantly reduced the percentage of PSF and SAF of catecholamine secretion in response to AngII stimulation, whereas the phosphorylation-deficient mutant Y¹⁴⁵F showed no significant effects compared to that of the wild type (Fig 7E–G, and Appendix Figs S9 and S10).

In order to investigate the mechanism underlying the phosphorylation of MUNC18-1 Y¹⁴⁵ as well as the disease-related mutant Y¹⁴⁵H in the regulation of hormone secretion, we compared the interactions of wild-type and mutant MUNC18-1 with the binding partner SYNTAXIN1 (Lim *et al*, 2013). Importantly, both the phosphorylation mimic mutant MUNC18-1-Y¹⁴⁵E and the disease-related mutant Y¹⁴⁵H significantly impaired the interaction between MUNC18-1 and SYNTAXIN1 (Fig 7H, Appendix Fig S10C). The effects of MUNC18-1 phospho-mimic Y¹⁴⁵E or phospho-defective Y¹⁴⁵F mutants on fusion pore dynamics are correlated with their abilities for interaction with the SYNTAXIN1, thus indicating that the binding between the MUNC18-1 and SYNTAXIN1, which was controlled by the phosphorylation status of Y¹⁴⁵ of MUNC18-1, may play an important role in the formation of the fusion pore during catecholamine secretion. In

Figure 7. Dephosphorylations of MUNC18-1 at the pY¹⁴⁵ site and DYNAMIN2 at the pY¹²⁵ site by PTP-MEG2 determine the “foot” probability of catecholamine secretion from chromaffin cells.

- A Structural representation and location of MUNC18-1-Y¹⁴⁵ in the complex structure of MUNC18-1-SYNTAXIN1 (PDB: 3PUJ).
- B Detailed structural representation of MUNC18-1-Y¹⁴⁵ and its interactive residues. Y¹⁴⁵ of MUNC18-1 interacts with the main chain carboxylic oxygen of residues I⁵³⁹ and G⁵⁶⁸ and forms hydrophobic interactions with L⁶, I⁵³⁹, L¹⁴⁷, L¹⁷⁹, L¹⁸³, and L²³⁰ to tether the arc shape of the three domains of MUNC18-1 (PDB: 3PUJ).
- C Association analysis of SNPs of MUNC18-1 with human disease.
- D Interactions of the PTP-MEG2-trapping mutants with the MUNC18-1-Y¹⁴⁵ mutants and DYNAMIN2-Y¹²⁵ mutants. PC12 cells were transfected with FLAG-MUNC18-1-Y¹⁴⁵, FLAG-DYNAMIN2-Y¹²⁵ and different mutations of the FLAG-MUNC18-1-Y¹⁴⁵A, Y¹⁴⁵H, Y¹⁴⁵E or Y¹⁴⁵F, FLAG-DYNAMIN2-Y¹²⁵A, Y¹²⁵E, Y¹²⁵F, 24 h before stimulation with 100 nM AngII, respectively. The cell lysates were then incubated with GST beads-PTP-MEG2-D⁴⁷⁰A complex for 2 h with constant rotation. The potential PTP-MEG2 substrates were pulled down by GST beads, and their levels were examined by the FLAG antibody with Western blot.
- E Primary chromaffin cells were transduced with lentivirus containing the gene encoding wild-type MUNC18-1 or different mutants. These cells were stimulated with 100 nM AngII. The amperometric spikes were detected with electrochemical experiments. Typical amperometric traces are shown.
- F, G The percentages of pre-spike foot (F) and stand-alone foot (G) for wild-type MUNC18-1 or different mutants were calculated.
- H The MUNC18-1-Y¹⁴⁵ mutations decreased the interaction between MUNC18-1 and SYNTAXIN1. PC12 cells were transfected with plasmid encoding SYNTAXIN1. The proteins in cell lysates were pulled down with purified GST beads-MUNC18-1-Y¹⁴⁵ complex and the GST-MUNC18-1-Y¹⁴⁵H/E/F, and detected with SYNTAXIN1 antibody. The right histogram shows the quantified protein levels.
- I Primary chromaffin cells were transduced with lentivirus containing the gene encoding wild-type DYNAMIN2 or different mutants. These cells were stimulated with 100 nM AngII. The amperometric spikes were detected with electrochemical experiments. Typical amperometric traces are shown.
- J, K The percentages of pre-spike foot (J) and stand-alone foot (K) for wild-type DYNAMIN2 or different mutants were calculated.
- L Plasmids encoding DYNAMIN2 (DYNAMIN2-WT, DYNAMIN2-Y¹²⁵E or DYNAMIN2-Y¹²⁵F) and LYN-YFP, AT1aR-C-RLUC were co-transferred into HEK293 cells at 1:1:1 ratio. The BRET experiment was performed to monitor the mutation effects of DYNAMIN2 on AT1aR endocytosis in response to AngII (1 μM) stimulation.
- M The GTPase assay was performed to detect the GTPase activity of the DYNAMIN2-WT, DYNAMIN2-Y¹²⁵E, and DYNAMIN2-Y¹²⁵F. Purified DYNAMIN2 proteins were incubated with 5 μM GTP in the presence of 500 μM DTT for 90 min, followed by addition of GTPase-Glo™ Reagent and detection reagent. The luminescence was measured after 37-min incubation.
- N Phosphorylated Y¹²⁵ of DYNAMIN2 was identified by LC-MS/MS. The PTP-MEG2-D⁴⁷⁰A trapping mutant was used to pull down potential PTP-MEG2 substrates from the adrenal lysates after AngII stimulation. Trypsin-digested potential PTP-MEG2 substrates were subjected to LC-MS/MS analysis. The doubly charged peptide with m/z 725.06 matches VYSPHVLNLTLDLPGITK of DYNAMIN2 with Y¹²⁵ phosphorylation.

Data information: (F–H, J–M) * indicates MUNC18-1, DYNAMIN2 mutant overexpression group compared with the WT overexpression group. # indicates MUNC18-1, DYNAMIN2 overexpression group compared with the control group. *P < 0.05; **P < 0.01; ***P < 0.001 and #P < 0.05; ##P < 0.01; ###P < 0.001. N.S. means no significant difference. Data were from 6 (F, G, J, K, L, M) or 3 (H) independent experiments. All the data were analyzed using one-way ANOVA, and showed as the mean ± s.e.m.

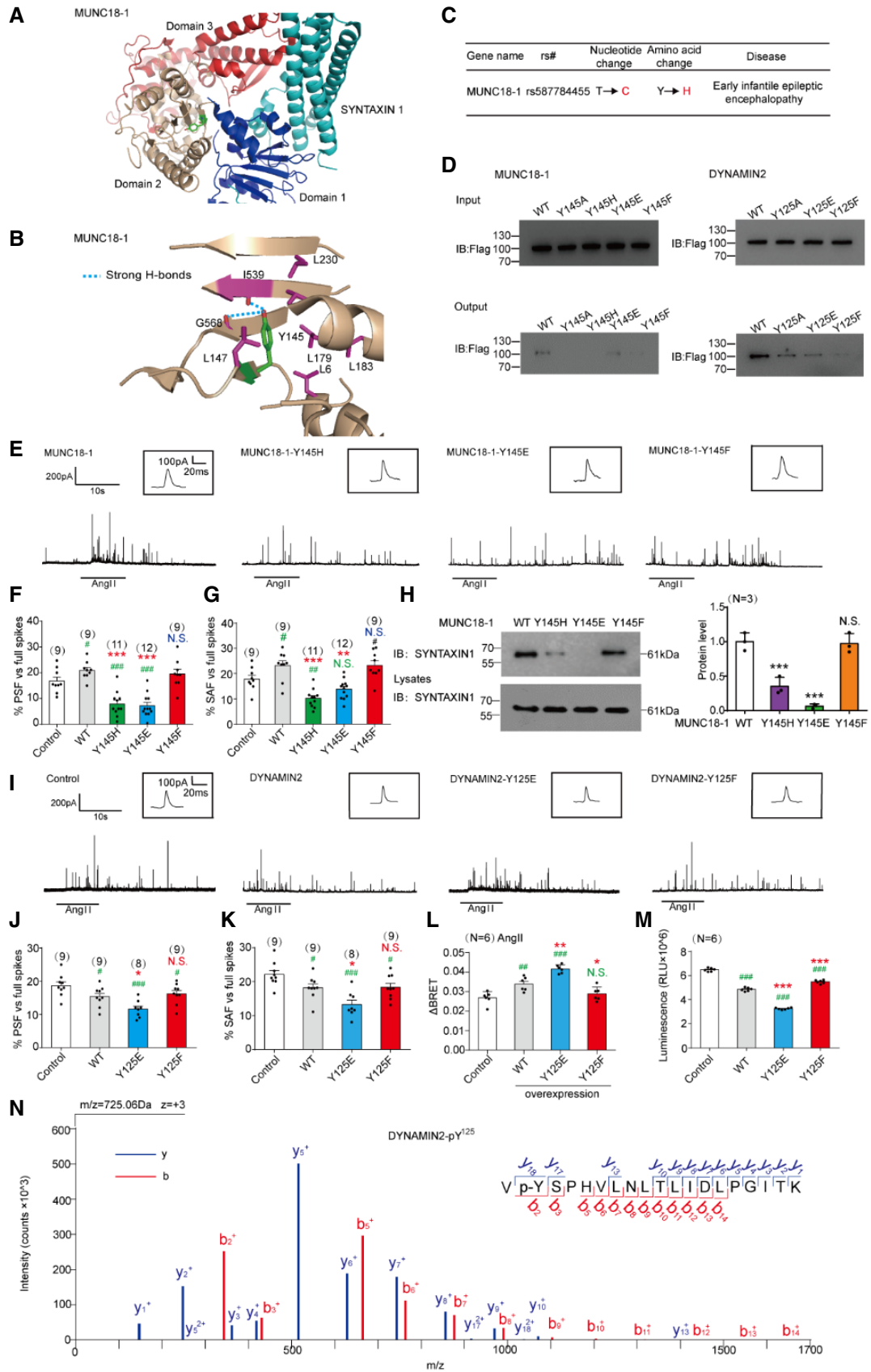


Figure 7.

contrast, the dephosphorylation of pY¹⁴⁵ of MUNC18-1 by PTP-MEG2 promoted initial pore opening and fusion. Collectively, these results suggested that the tyrosine phosphorylation of Y¹⁴⁵ impaired the initial opening of the fusion pore in agonist-induced catecholamine secretion in the primary chromaffin cells. This is probably through either disrupting the arc shape of MUNC18-1 or impairing the interaction between MUNC18-1 and Syntaxin1. In addition, the effects of the mutations of MUNC18-1 on protein stability were detected in response to cycloheximide (CHX) treatments. The results show that the mutations of MUNC18-1 had no significant influence on protein stability, which suggested that the influence of MUNC18-1 on “foot” parameters had no correlation with their degradation (Appendix Fig S12).

PTP-MEG2 regulated the initial opening of the fusion pore through dephosphorylating DYNAMIN2-pY¹²⁵

Besides MUNC18-1, two additional substrates of PTP-MEG2, the Y⁴⁵ site of VAMP7 and the Y¹²⁵ site of DYNAMIN2, were confirmed by GST pull-down assay (Fig 7D, Appendix Fig S8F–H). It was well known that DYNAMIN1 and DYNAMIN2, both active regulators of pore fusion dynamics, involved in the pore establishment, stabilization, constriction, and fission processes (Zhao *et al.*, 2016; Jones *et al.*, 2017; Shin *et al.*, 2018). The dephosphorylation site of DYNAMIN2 by PTP-MEG2, the Y¹²⁵, is located in a β -sheet of DYNAMIN GTPase domain according to the DYNAMIN1 structure (PDB ID: 5D3Q). Previous studies have identified that phosphorylation of DYNAMIN close to the G domain significantly increased its GTPase activity, thus promoted endocytosis (Kar *et al.*, 2017). We hypothesized that the phosphorylation of the DYNAMIN2 pY¹²⁵ site increased pore fission by up-regulating its GTPase activity, whereas dephosphorylation of DYNAMIN2 pY¹²⁵ site by PTP-MEG2 reversed it. Consistent with the negative regulation role of DYNAMIN2 on pore fusion, the primary chromaffin cells transduced by lentivirus encoding DYNAMIN2 wild type and the Y¹²⁵F mutant significantly decreased the percentage of the PSF and SAF of catecholamine secretion elicited by AngII. Importantly, the phosphorylation mimic mutant DYNAMIN2 Y¹²⁵E exhibited significantly more reduction on

the PSF and SAF percentage compared to that of the wild-type DYNAMIN, indicating that the DYNAMIN Y¹²⁵E is a gain of function mutant (Fig 7I–K, Appendix Fig S11). It has been demonstrated that the DYNAMIN-mediated pore fission process is closely correlated with the receptor endocytosis. In accordance with their effects on percentage of PSF and SAF, overexpression of the DYNAMIN2 wild type or Y¹²⁵E phospho-mimic mutant markedly increased the AngII-induced AT1aR endocytosis (Fig 7L; Liu *et al.*, 2017). The *in vitro* GTPase activity further suggested that the phosphorylation of DYNAMIN2 at pY¹²⁵ site up-regulated its activity (Fig 7M). Moreover, the LS-MS/MS verified the phosphorylation of DYNAMIN2 at pY¹²⁵ site in primary adrenal medulla under AngII stimulation (Fig 7N, Appendix Table S4). Collectively, these results indicated that DYNAMIN2 pY¹²⁵ phosphorylation occurred under AngII stimulation and negatively regulated the percentage of PSF and SAF of the AngII-induced catecholamine secretion through increase the GTPase activity of DYNAMIN2. In addition, the effects of the mutations of DYNAMIN2 on protein stability were detected in response to cycloheximide (CHX) treatments. The results show that the mutations of DYNAMIN2 had no significant influence on protein stability, which suggested that the influence of DYNAMIN2 on “foot” parameters had no correlation with their degradation (Appendix Fig S12).

Molecular mechanisms of the interaction between PTP-MEG2/MUNC18-1-pY¹⁴⁵ and interaction between the PTP-MEG2/DYNAMIN2-pY¹²⁵

The k_{cat}/K_m of PTP-MEG2 toward a phospho-segment derived from MUNC18-1-pY¹⁴⁵ is very similar to that obtained with a phospho-segment derived from the known substrate pY⁸³ site of NSF (Appendix Table S1 and Appendix Table S5). We therefore crystallized the PTP-MEG2 trapping mutant with the MUNC18-1-E¹⁴¹-pY¹⁴⁵-S¹⁴⁹ phospho-segment and determined the complex structure at 2.2 Å resolution (Table 1). The 2Fo-Fc electro-density map allowed the unambiguous arrangement of seven residues of the phospho-MUNC18-1-E¹⁴¹-pY¹⁴⁵-S¹⁴⁹ segment in the crystal structure (Fig 8A). Importantly, comparing with the phospho-NSF-E⁷⁹-pY⁸³-K⁸⁷ segment, the phospho-MUNC18-1-E¹⁴¹-pY¹⁴⁵-S¹⁴⁹ displayed

Figure 8. The structural details of the PTP-MEG2-MUNC18-1-Y¹⁴⁵ interaction and catalytic bias of PTP-MEG2 toward NSF-pY⁸³ and MUNC18-1-pY¹⁴⁵.

- The 2Fo-Fc annealing omit map (contoured at 1.0 σ) around MUNC18-1-pY¹⁴⁵ phospho-segment.
- Comparison of residues of PTP-MEG2 interacting with NSF and MUNC18-1. Amino acid residues of NSF and MUNC18-1 are colored as follows: green, residues interacting with both NSF and MUNC18-1; red, residues specifically contributing to NSF recognition; and blue, residues selectively contributing to MUNC18-1 interaction.
- The structural alteration of the interactions surrounding Y⁴⁷¹ of PTP-MEG2 with the MUNC18-1-pY¹⁴⁵ site.
- The structural alteration of the interactions surrounding I⁵¹⁹ of PTP-MEG2 with the MUNC18-1-pY¹⁴⁵ site.
- Relative phosphatase activities of different PTP-MEG2 mutants toward the MUNC18-1-pY¹⁴⁵ phospho-segment compared with wild-type PTP-MEG2.
- Relative phosphatase activities of different PTP-MEG2 mutants toward the DYNAMIN 2-pY¹²⁵ phospho-segment compared with wild-type PTP-MEG2.
- The percentages of PSF and SAF for PTP-MEG2-R⁴⁰⁹A or R⁴¹⁰A were calculated.
- Schematic illustration of the PTP-MEG2-regulated processes of vesicle fusion and secretion in chromaffin cells via the dephosphorylation of different substrates with distinct structural basis. PTP-MEG2 regulates vesicle fusion and vesicle size during the catecholamine secretion of adrenal gland by modulating the phosphorylation state of the pY⁸³ site of NSF, which relies on the key residues G³³⁴, D³³⁵ (pY loop), Y⁴⁷¹ (WPD loop), I⁵¹⁹ (P-loop), and Q⁵⁵⁹ (Q loop). PTP-MEG2 regulates the fusion pore initiation and expansion procedures of catecholamine secretion by the adrenal gland (also designated as foot probability) by modulating the newly identified substrate MUNC18-1 at its pY¹⁴⁵ site and DYNAMIN2 at its pY¹²⁵, through distinct structural basis from that of its regulation of NSF phosphorylation.

Data information: (E, F) Residues are colored according to Fig 8B. (E, F), * $P < 0.05$, ** $P < 0.01$, *** $P < 0.001$: PTP-MEG2 mutants compared with the control. N.S. means no significant difference. Data were obtained from 3 independent experiments. (G), * indicates PTP-MEG2-R⁴⁰⁹A or R⁴¹⁰A mutant overexpression group compared with the WT overexpression group. # indicates the PTP-MEG2 overexpression group compared with the control group. ** $P < 0.01$; *** $P < 0.001$ and ### $P < 0.01$; ### $P < 0.001$. N.S. means no significant difference. Data were obtained from 10 cells in each group of 6 independent experiments. All the data were analyzed using one-way ANOVA and showed as the mean \pm s.e.m.

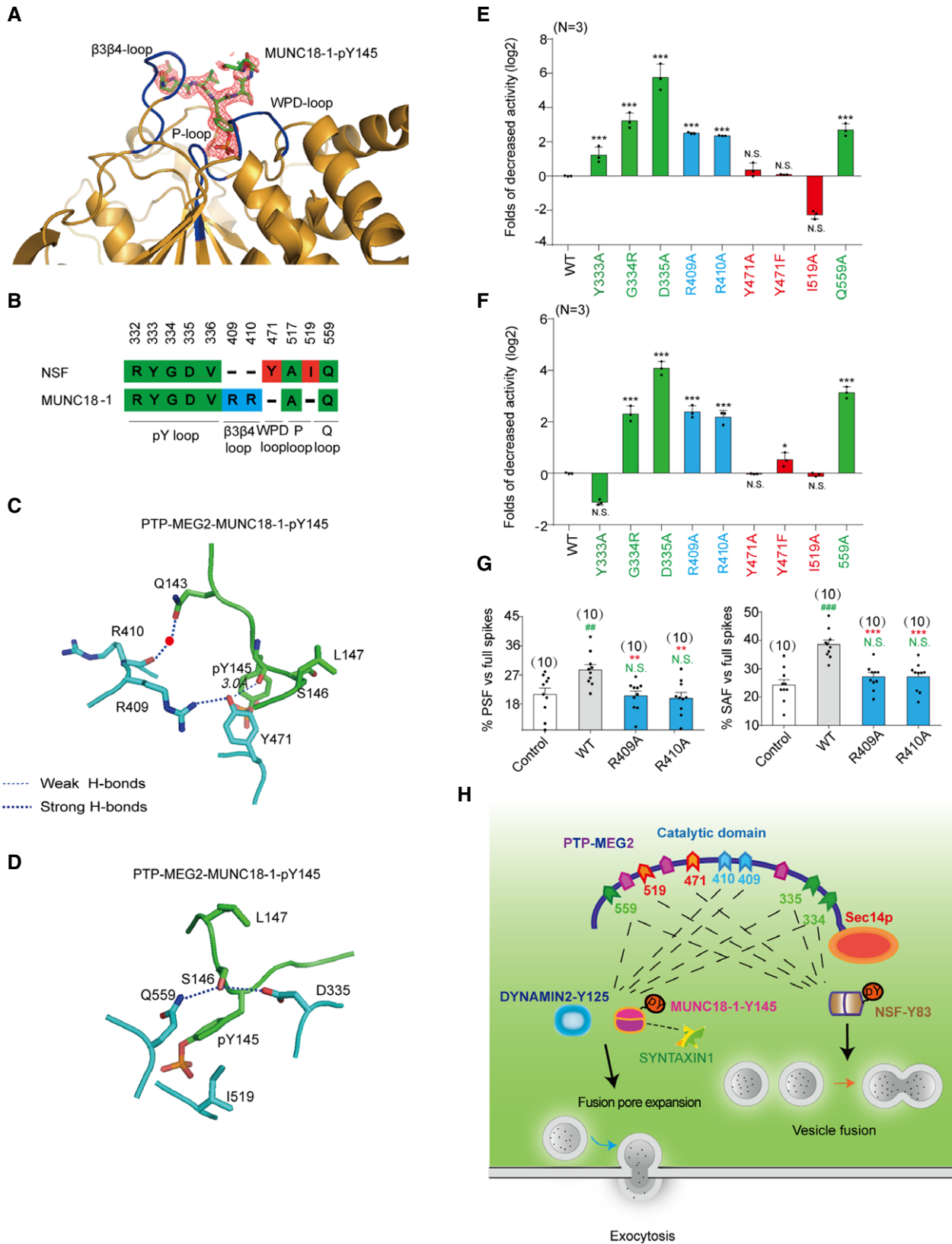


Figure 8.

different interaction patterns with the residues in the PTP-MEG2 active site, forming new interactions with R⁴⁰⁹ and R⁴¹⁰ but lost interactions with Y⁴⁷¹ and I⁵¹⁹ (Fig 8B). Whereas PTP-MEG2 Y⁴⁷¹ formed extensive hydrophobic interactions with NSF-T⁸⁴ and NSF-F⁸⁵, as well as a well-defined hydrogen bond (2.4 Å) with the carbonyl oxygen of NSF-pY⁸³, PTP-MEG2 Y⁴⁷¹ formed only a weaker H-bond with the carbonyl oxygen of MUNC18-1-pY¹⁴⁵ due to a 0.62 Å shift of Y⁴⁷¹ away from the central pY substrate (Fig 8C, Appendix Fig S13A). Similarly, PTP-MEG2 I⁵¹⁹ did not form specific interactions with the MUNC18-1-E¹⁴¹-pY¹⁴⁵-S¹⁴⁹ segment except for the central pY. In contrast, PTP-MEG2 I⁵¹⁹ formed specific hydrophobic interactions with NSF-T⁸⁴ (Fig 8D, Appendix Fig S13B). Consistently, mutations of PTP-MEG2 Y⁴⁷¹A, Y⁴⁷¹F, or I⁵¹⁹A significantly decreased the phosphatase activity toward the phospho-NSF-E⁷⁹-pY⁸³-K⁸⁷ segment (Fig 3C) but had no significant effect on the phospho-segments derived from both MUNC18-1-pY¹⁴⁵ and DYNAMIN2 pY¹²⁵ sites (Fig 8E and F, Appendix Table S5). Meanwhile, R⁴⁰⁹A and R⁴¹⁰A mutations substantially decreased the catalytic activity toward phospho-segments derived from both MUNC18-1-pY¹⁴⁵ and DYNAMIN2 pY¹²⁵ sites. This indicated that recognition of these substrates was mediated by common residues (Fig 8E and F, Appendix Table S5). Notably, the PTP-MEG2 catalytic domain mutations showed no significant effects on the interactions between PTP-MEG2 with the NSF, MUNC18-1, and DYNAMIN2. This indicated that other domain of PTP-MEG2, such as its sec14p domain, participated in the association of PTP-MEG2 with these proteins (Appendix Figs S5G and S13C–F). With electrochemical studies, we further demonstrated that R⁴⁰⁹A and R⁴¹⁰A mutations decreased the probability of both PSF and SAF (Fig 8G, Appendix Fig S14). It is worth to note that PTP-MEG2 Y⁴⁷¹A, Y⁴⁷¹F, and I⁵¹⁹A affect only the spike number and amount, but not the foot probability (Fig 5B–G). Collectively, our data suggested that PTP-MEG2 regulated intracellular vesicle fusion by modulating the NSF-pY⁸³ phospho-state but regulated the process of vesicle fusion pore initiation by dephosphorylating MUNC18-1 at pY¹⁴⁵ site and DYNAMIN2 at pY¹²⁵ site (Fig 8H).

Discussion

Post-translational modifications of secretion machinery proteins are known as powerful ways to regulate exocytosis. In contrast to the well-characterized serine/threonine phosphorylation, the importance of tyrosine phosphorylation in exocytosis has only recently begun to be appreciated (Seino *et al*, 2009; Jewell *et al*, 2011; Cijssouw *et al*, 2014; Laidlaw *et al*, 2017; Meijer *et al*, 2018; Gabel *et al*, 2019). In addition to the phosphorylation of NSF at its pY⁸³ site, recent studies have shown that tyrosine phosphorylation of MUNC18-3 at the pY²¹⁹ and pY⁵²⁷ sites, Annexin-A2 at pY²³, and MUNC18-1 at pY⁴⁷³ actively participates in the vesicle release machinery to explicitly regulate exocytosis processes (Jewell *et al*, 2011; Meijer *et al*, 2018; Gabel *et al*, 2019). The tyrosine phosphorylation at specific sites of the signaling molecule is precisely regulated by protein tyrosine kinases and protein tyrosine phosphatases (Tonks, 2006; Yu & Zhang, 2018). Although tyrosine kinases such as the insulin receptor, Src, and Fyn are acknowledged to play critical roles in hormone secretion (Jewell *et al*, 2011; Soares *et al*, 2013; Meijer *et al*, 2018; Oakie & Wang, 2018), only a very few PTPs that

regulate the vesicle release machinery have been identified, and the structural basis of how these PTPs selectively dephosphorylate the key tyrosine phosphorylation sites governing exocytosis was unknown. In the current study, we demonstrated that PTP-MEG2 is an important regulator of hormone secretion from the chromaffin cell, using a selective PTP-MEG2 inhibitor in combination with cellular and electrochemical amperometric recording. The current study extended the regulatory role of PTP-MEG2 in various steps of exocytosis in hormone secretion beyond the previously known simple vesicle fusion step of the immune system (Huynh *et al*, 2004). We then determined the crystal structure of PTP-MEG2 in complex with the pY⁸³ phospho-segment of the NSF, the key energy provider for disassembling fusion-incompetent cis SNARE complexes in the process of vesicle fusion in immunocytes (Huynh *et al*, 2004). The complex structure not only revealed the structural rearrangement in PTP-MEG2 in response to binding of the substrate NSF and identified Q⁵⁵⁹:D³³⁵ as the key pair for substrate specificity of the pY + 1 site, but also provided clues that PTP-MEG2 regulated the initial opening of the fusion pore through another unknown substrate. Fortunately, we were able to deduce the signature of the pY + 1 and pY + 2 positions of this unknown substrate by carefully inspecting the PTP-MEG2/phospho-NSF-E⁷⁹-pY⁸³-K⁸⁷ complex structure and analyzing the functional data of the PTP-MEG2 interface mutants. Further bioinformatics studies and cellular and physiological experiments enabled us to discover that PTP-MEG2 regulates the initial opening of the fusion pore by modulating the tyrosine phosphorylation states of MUNC18-1 at the pY¹⁴⁵ site and DYNAMIN2 at the pY¹²⁵ site. Therefore, we have revealed that PTP-MEG2 regulates different steps of the exocytosis processes via dephosphorylating distinct substrates. PTP-MEG2 regulates the vesicle size and vesicle-vesicle fusion step by dephosphorylating NSF at its NSF-pY⁸³ site, whereas it regulates the process of LDCV fusion pore initiation and expansion by controlling specific phosphorylation sites of MUNC18-1 and DYNAMIN2. Moreover, our studies highlight that the combination of structural determination and functional delineation of the interface mutants of the protein complex is a powerful approach to characterizing the signaling events and identifying unknown downstream signaling molecules.

Fusion pore opening and expansion is thought to be a complex process requiring the docking of apposed lipid bilayers and involvement of multiple proteins to form a hemi-fusion diaphragm including SNAREs, MUNC18-1, and DYNAMIN (Sudhof & Rothman, 2009; Hernandez *et al*, 2012; Mattila *et al*, 2015; Baker & Hughson, 2016; Zhao *et al*, 2016; Jones *et al*, 2017). Dissection of the molecular mechanism underlying pore fusion dynamics in exocytosis is challenging because direct observation of this process is difficult to achieve due to the short expansion time and the tiny size of the pore (Hong & Lev, 2014; Baker & Hughson, 2016; Gaisano, 2017). Importantly, the DYNAMINs are key terminators of the fusion pore expansion by scissoring vesicles from the cell membrane (Eitzen, 2003; Zhao *et al*, 2016; Jones *et al*, 2017; Shin *et al*, 2018). The large-scale phosphoproteomic screens have identified multiple tyrosine phosphorylation sites of DYNAMIN, such as that occurring at pY⁸⁰, pY¹²⁵, pY³⁵⁴, and pY⁵⁹⁷ sites (Ballif *et al*, 2008; Mallozzi *et al*, 2013). Among them, the Y⁵⁹⁷ was a well-studied phosphorylation site of DYNAMIN, which was previously reported to increase self-assembly and GTP hydrolysis in both DYNAMIN1 and 2 (Kar *et al*, 2017). However, the Y⁵⁹⁷ of DYNAMIN was probably not the target of PTP-

MEG2 because the interaction of Y⁵⁹⁷ or A⁵⁹⁷ with PTP-MEG2 exhibited no significant differences. However, the regulation of other tyrosine phosphorylation site, such as pY¹²⁵, as well as how this particular tyrosine phosphorylation participated in a selective secretion process, has not been elucidated previously. Here, by using pharmacological approach with high selectivity, functional alanine mutagenesis according to structural characterization, combined with bioinformatics, electrochemistry and enzymology, we have demonstrated that PTP-MEG2 negatively regulated the pY¹²⁵ phosphorylation state of DYNAMIN2 during the catecholamine secretion, which promoted the cessation of the fusion pore expansion through increasing its GTPase activity.

In addition to DYNAMIN, MUNC18-1 and its closely related subfamily members have been demonstrated to participate in several processes during vesicle secretion by interacting with SNAREs, such as docking, priming, and vesicle fusion (Fisher *et al*, 2001; Korteweg *et al*, 2005; Gulyas-Kovacs *et al*, 2007; Ma *et al*, 2013; Cijssouw *et al*, 2014; Ma *et al*, 2015; Chai *et al*, 2016; He *et al*, 2017; Sitariska *et al*, 2017; Meijer *et al*, 2018). Importantly, the tyrosine phosphorylation of MUNC18-1 at Y⁴⁷³ was recently reported as a key step in modulating vesicle priming by inhibiting synaptic transmission and preventing SNARE assembly (Meijer *et al*, 2018). In addition, the tyrosine phosphorylation of MUNC18-3 on Y⁵²¹ was essential for the dissociation of MUNC18-3 and SYNTAXIN4 (Umahara *et al*, 2008). Moreover, the dephosphorylation of MUNC18-1-Y¹⁴⁵ was suggested to be essential in maintaining the association between MUNC18-1 and SYNTAXIN1 (Lim *et al*, 2013). In the present study, we demonstrated that the MUNC18-1 Y¹⁴⁵E phosphomimic mutation, but not the non-phosphorylated mutation Y¹⁴⁵F, significantly decreased the PSF and the SAF probability in cultured primary chromaffin cells. Notably, either the Y¹⁴⁵E phosphomimic mutation or the epileptic encephalopathy associated Y¹⁴⁵H mutant disrupted their interactions with SYNTAXIN1. Structural inspection also suggested that both phosphorylation of Y¹⁴⁵ and Y¹⁴⁵H mutant could destabilize the arc shape of native MUNC18-1. Therefore, it is very likely that either the association of the MUNC18-1 with the SYNTAXIN1 or the maintenance of the arc shape of the MUNC18-1 actively participated in initial pore opening and expansion. Future studies by solving the fusion machinery structures encompassing the MUNC18-1 at different stages with high resolutions, as well as more detailed fusion pore dynamics analysis using *in vitro* reconstitution system, could provide deeper insights for these key events in pore fusion processes. In the present study, the structural and enzymatic analysis of PTP-MEG2 in complex with MUNC18-1-pY¹⁴⁵ confirmed that PTP-MEG2 regulated two different substrates, the MUNC18-1-pY¹⁴⁵ and the DYNAMIN2-pY¹²⁵, which presented similar structural features recognized by PTP-MEG2 and generated similar effects on fusion pore dynamics. Therefore, our studies exemplified how a PTPase regulated one important physiological process through two different substrates. This added new information of the fusion pore regulation from another aspect.

Notably, the MUNC18-1 Y¹⁴⁵H mutation is a known SNP that is associated with epileptic encephalopathy (Stamberger *et al*, 2017). Y¹⁴⁵H behaves similarly to the MUNC18-1 phosphorylation mimic mutant Y¹⁴⁵E by disrupting its interaction with SYNTAXIN1 and reducing the probability of PSF elicited by AngII stimulation in primary chromaffin cells. This observation provided a clue for the pathological effects of the MUNC18-1 Y¹⁴⁵H mutation. In addition to

MUNC18-1, we found that VAMP7 interacted with PTP-MEG2 via their Y⁴⁵ tyrosine phosphorylation site, respectively. DYNAMIN1, PASCIN1, and SNAP25 are also potential substrates of PTP-MEG2 depending on specific cellular contexts. The functions of VAMP7 phosphorylation at the Y⁴⁵ site and its dephosphorylation by PTP-MEG2 in the exocytosis process await further investigation.

Finally, by solving the two crystal structures of PTP-MEG2 in complex with two substrates, the phospho-NSF-E⁷⁹-pY⁸³-K⁸⁷ segment and the phospho-MUNC18-1-E¹⁴¹-pY¹⁴⁵-S¹⁴⁹ segment, we revealed that PTP-MEG2 recognized these functionally different substrates through distinct structural bases. Whereas K⁴¹¹, Y⁴⁷¹, and I⁵¹⁹ contributed most to the selective interaction of PTP-MEG2 with NSF, another set of residues, including R⁴⁰⁹ and R⁴¹⁰, mediated the specific binding of PTP-MEG2 to MUNC18-1 (Fig 8B). Most importantly, mutating Y⁴⁷¹ and I⁵¹⁹ to A significantly decreased the activity of PTP-MEG2 toward the phospho-NSF-E⁷⁹-pY⁸³-K⁸⁷ segment but not the phospho-MUNC18-1-E¹⁴¹-pY¹⁴⁵-S¹⁴⁹ segment. The biochemical data lined up with the functional data that PTP-MEG2 Y⁴⁷¹A and I⁵¹⁹A of PTP-MEG2 affected the vesicle fusion procedure only but not the fusion pore opening and expansion processes. These data not only indicate that PTP-MEG2 regulates different steps of exocytosis through different substrates in an explicit temporal and spatial context but also afforded important guidance for the design of selective PTP-MEG2 inhibitors according to the different interfaces between PTP-MEG2 and its substrates to explicitly regulate specific physiological processes, supporting the hypothesis of “substrate-specific PTP inhibitors” (Doody & Bottini, 2014). The design of such inhibitors will certainly help to delineate specific roles of PTP-MEG2 in different physiological and pathological processes.

In conclusion, we have found that PTP-MEG2 regulates two different processes of exocytosis during catecholamine secretion, namely, vesicle fusion and the opening and extension of the fusion pore, through two different substrates with distinct structural bases. We achieved this knowledge by determining the complex structure and performing functional delineation of the protein complex interface mutants. The present study supports the hypothesis that the tyrosine phosphorylation of secretion machinery proteins is an important category of regulatory events for hormone secretion and is explicitly regulated by protein tyrosine phosphatases, such as PTP-MEG2. Dissecting the molecular and structural mechanisms of such modulation processes will provide an in-depth understanding of the exocytosis process and guide further therapeutic development for exocytosis-related diseases, such as epileptic encephalopathy (Stamberger *et al*, 2017).

Materials and Methods

Cells and agents

The HEK293 cell lines, the 293T cell lines, and PC12 cell lines were originally obtained from the American Type Culture Collection (ATCC). The HEK293 cell lines and 293T cell lines were grown in DMEM with 10% FBS (Gibco, Grand Island, NY, US) and 1% penicillin/streptomycin at 37°C. PC12 cells were maintained at 37°C in DMEM containing 10% FBS (Gibco, US), 5% donor equine serum (Gibco, US), and 1% penicillin/streptomycin. The information of agents and softwares is displayed in Appendix Table S6.

Constructs

Sequences of PTP-MEG2 catalytic domain were subcloned into PET-15b expression vector with an N-terminal His tag or PGEX-6P-2 expression vector containing an N-terminal GST tag. The mutations of PTP-MEG2 were constructed by the QuikChange kit from Stratagene. The information of constructs and primers is detailed in Appendix Table S7.

Recombinant lentivirus construction and lentivirus infection

For recombinant lentivirus packaging, the construction and infection was carried out as previously reported (Zhang *et al.*, 2018). Plasmids carrying different genes including pCDH-PTP-MEG2-G³³⁴R/D³³⁵A/Y⁴⁷¹A/Y⁴⁷¹F/I⁵¹⁹A/Q⁵⁵⁹A/R⁴⁰⁹A/R⁴¹⁰A/WT-GFP, pCDH-MUNC18-1-Y¹⁴⁵H/Y¹⁴⁵E/Y¹⁴⁵F/WT-GFP, and pCDH-DYNAMIN2-Y¹²⁵E/Y¹²⁵F/WT-GFP were transfected into 293T cells using Lipofectamine TM 2000 (Thermo Fisher, Waltham, MA, USA) according to the manufacturer's instructions. Three days after transfection, the supernatant of virus encoding PTP-MEG2, MUNC18-1, or DYNAMIN2 was collected and filtered. The PTP-MEG2, MUNC18-1, or DYNAMIN2 lentivirus (1×10^6 TU/ml) was used to infect the primary chromaffin cells in later experiments.

ELISA

Freshly isolated adrenal medullas from adult female mice (6–8 weeks) were cultured in DMEM containing 1% penicillin/streptomycin and 10% FBS. After 2 h of starvation, adrenal medullas were stimulated with high KCl (70 mM) or AngII (100 nM) for 1 min, with or without pre-incubation of a specific PTP-MEG2 inhibitor (400 nM) for 1 h. The supernatants were collected, and the epinephrine or norepinephrine secretion was determined by using the Epinephrine or norepinephrine ELISA kit (Shanghai Jianglai Co., Ltd, JL11194-48T/JL13969-96T) according to the manufacture's protocol.

Primary chromaffin cells and animal ethics

Adrenal medullas were freshly isolated from adult female C57BL/6 mice (6–8 weeks) and placed in cold D-Hank's buffer (PH 7.2, 109.5 mM NaCl, 23.8 mM NaHCO₃, 10.0 mM D-Glucose, 5.36 mM KCl, 17.72 mM H-HEPE, 10.07 mM NaH₂PO₄, 7.28 mM Na-HEPE). The adipose tissue was separated in cold D-Hank's buffer. Then, the adrenal cortex was isolated and discarded. The adrenal medulla should be isolated as quickly as possible and then the medulla was cut into 4 pieces. The medulla was transferred to 1 ml Papain solution and placed in an incubator at 37°C for digestion for 10 min (the mixture should be reversed at 5 min). After that, the enzyme solution was absorbed and discarded and then changed to fresh Papain solution for further digestion for 10 min (the mixture should be reversed at 5 min). D-Hank's buffer was added to terminate digestion. Adding 100–200 μ l D-Hank's buffer, start gently pipetting cells 20 times and then discard the supernatant (repeated 3 times). 50–100 μ l D-Hank's buffer was again added and cells were pipetted 20 times. After that, the supernatant was collected and spreaded (repeated until the precipitate disappeared) and put it into the incubator at 37°C for 30 min to resuspend the chromaffin cells. D-Hank's buffer was then discarded and replaced with 2 ml DMEM. The

relevant experimental operation was completed within 48 h. The animal experiments were approved and supervised by the Animal Ethics Committee of Shandong University (No. LL-201602037).

Quantitative real-time PCR

Adrenal medullas were freshly isolated from adult female mice (6–8 weeks). The lentivirus encoding wild type or mutants of PTP-MEG2, MUNC18-1 or DYNAMIN2 (1×10^6 TU/ml) were used to infect the primary chromaffin cells. On the third day, about 10–20 pheochromaffin cells with different brightness were selected in each plate under the fluorescence microscope and the fluorescence photographs were taken. After classification by different brightness, the cells were glued with the tips of ultra-fine glass tubes, and the tips of glass tubes with the cells were directly broken in the PCR tube. The PCR tube was preloaded with 5 μ l RNA enzyme inhibitors (Invitrogen, 10777019). 1 μ l DNA scavenger was added to the PCR tube, which was left at room temperature for half an hour and then terminated with a terminator. The purpose of this step is to remove the interference of genomic DNA. All the samples were reverse-transcribed using the Revertra Ace qPCR RT Kit (TOYOBO FSQ-101) to obtain cDNA. Then, the quantitative real-time PCR was performed with the LightCycler apparatus (Bio-Rad) using the FastStart Universal SYBR Green Master (Roche). The expression of actin was used as a control. The primer sequences are detailed in Appendix Table S8.

Electrochemical amperometry

5- μ m glass carbon fiber electrode (CFE) was used to measure quantal CA released from the mouse adrenal medulla chromaffin cell as previously described (Liu *et al.*, 2017). We used a Multiclamp 700B amplifier (2012, Axon, Molecular Devices, USA) to perform electrochemical amperometry, which interfaced to Digidata 1440A with the pClamp 10.2 software (Liu *et al.*, 2017). The holding potential of 780 mV was used to record the amperometric current (*I*_{amp}). All experiments were performed at room temperature (20–25°C). The CFE surface was positioned in contact with the membrane of clean primary chromaffin cells to monitor the quantal release of the hormone containing catecholamine substances. In our kinetic analysis of single amperometric spike, we only used the amperometric spikes with S/N > 3 (signal/noise). The standard external solution for our amperometry measurement is as follows: 5 mM KCl, 10 mM glucose, 10 mM HEPES pH 7.4, 2 mM CaCl₂, 150 mM NaCl, and 2 mM MgCl₂. We analyzed all data using Igor (WaveMetrics, Lake Oswego, Oregon) and a custom-made macro program. Statistical data were given as the mean \pm s.e.m. and analyzed with one-way ANOVA.

Electron microscopy

The female mice (6–8 weeks) were decapitated, and the adrenal medullas were freshly isolated and cut to 150- μ m-thick sections. The sections were immersed in Ringer's saline (125 mM NaCl, 2.5 mM KCl, 1.25 mM NaH₂PO₄, 26 mM NaHCO₃, 10 mM D-Glucose, 2 mM CaCl₂, 1 mM MgCl₂) for 40 min at room temperature. During this period, continuous gases of 5% CO₂ and 95% O₂ were offered to the saline to ensure the survival of the tissue slice. After 40 min of starvation, the sections were stimulated with

different conditions (control; only 100 nM AngII agonists for 1 min; only 400 nM PTP-MEG2 inhibitor for 45 min; 100 nM AngII agonists and 400 nM PTP-MEG2 inhibitor for 1 or 45 min) at 37°C, respectively. These sections were firstly immersed in precooled 3% glutaraldehyde and fixed at 4°C for 2 h, and then rinsed in PBS isotonic buffer, with repeated liquid exchanges and cleaning overnight, so that the samples were thoroughly rinsed and soaked in the buffer. After rinsing, the sample was fixed at 4°C with 1% osmium acid for 2 h. It was rinsed with isosmotic buffer solution at 0.1 M PBS for 15 min. The sections were dehydrated with ethanol at concentrations of 50, 70, and 90%, then ethanol at concentration of 90% and acetone at concentration of 90%, and at last only acetone at concentrations of 90 and 100%. We then replaced the acetone with the Epon gradually. The sections were added to Epon and polymerized at 60°C for 36 h. Ultra-thin sections were performed at the thickness of 60 nm by the LKB-1 ultra microtome, and then the ultra-thin sections were collected with the single-hole copper ring attached with formvar film. The sample was stained with 2% uranium acetate for 30 min and then stained with 0.5% lead citrate for 15 min. These prepared samples were examined by JEM-1200EX electron microscope (Japan).

Western

Cells or medulla sections were lysed in lysis buffer (50 mM Tris pH 8.0, 150 mM NaCl, 1 mM NaF, 1% NP-40, 2 mM EDTA, Tris-HCl pH 8.0, 10% glycerol, 0.25% sodium deoxycholate, 1 mM Na₃VO₄, 0.3 μM aprotinin, 130 μM bestatin, 1 μM leupeptin, 1 μM pepstatin, and 0.5% IAA) after rinsing with the pre-chilled PBS on ice. Cell and tissue lysates were kept on ice for 35 min and then sediment via centrifugation (10,800 g) for 15 min at 4°C. The whole-cell and tissue protein lysate samples (30 μg) were prepared for SDS-PAGE. The proteins in the gel were transferred to a nitrocellulose filter membrane by electro blotting and then probed with the appropriate primary and secondary antibodies. Antibody binding was detected by an HRP system.

Immunofluorescence

For the acquisition of tissue cells used in immunofluorescence, the Wistar rats were decapitated, and the adrenal medullas were freshly isolated (female mice, 6–8 weeks). The isolated adrenal medullas were incubated in 100 nM AngII for 1 min and then immersed in 4% paraformaldehyde for fixation overnight at 4°C. Then, the fixed tissues were washed for 4 h in PBS containing 10% sucrose at 4°C for 8 h in 20% sucrose and in 30% sucrose overnight. Then, these adrenal medullas were imbedded in Tissue-Tek OCT compound and then mounted and frozen them at -25°C. Subsequently, the adrenal medulla was cut to 4-μm-thick coronal serial sections. The adrenal medullas sections were blocked with 1% (vol/vol) donkey serum, 2.5% (wt/vol) BSA, and 0.1% (vol/vol) Triton X-100 in PBS for 1.5 h. Then, the slides were incubated with primary antibodies against PTP-MEG2 (1:100), NSF (1:50), MUNC18-1 (1:50), VAMP7 (1:50), DYNAMIN2 (1:100), SNAP25 (1:100), and PACSIN1 (1:50) at 4°C overnight. After washing with PBS for 3 times, the slides were incubated with the secondary antibody (1:500) for 1 h at room temperature. The slides were stained with DAPI (1:2,000). Images were captured using a confocal

microscope (ZEISS, LSM780). Pearson's co-localization coefficients were analyzed with Image-Pro Plus.

K_m and k_{cat} measurements

Enzymatic activity measurement was carried out as previously reported (Wang *et al*, 2014; Li *et al*, 2016). The standard solution (DMG buffer) for our enzymatic reactions is as follows: 50 mM 3, 3-dimethyl glutarate pH 7.0, 1 mM EDTA, and 1 mM DTT. The ionic strength was maintained at 0.15 M (adjusted by NaCl). For the pNPP activity measurement, 100 μl reaction mixtures were set up in a total volume in a 96-well polystyrene plate (Thermo Fisher Scientific, Waltham, MA, US). The substrate concentration ranging from 0.2 to 5 K_m was used to determine the k_{cat} and K_m values. Reactions were started by the addition of an appropriate amount of His-PTP-MEG2-CD-WT or corresponding mutants, such as Y³³³A, G³³⁴R, D³³⁵A, Y⁴⁷¹A, Y⁴⁷¹F, I⁵¹⁹A, Q559A, R⁴⁰⁹A, and R⁴¹⁰A. The dephosphorylation of pNPP was terminated by adding 120 μl 1 M NaOH, and the enzymatic activity was monitored by measuring the absorbance at 405 nm. The activities toward phospho-peptide segment derived from NSF or MUNC18-1 were measured as following: In the first column, 90 μl diluted NSF/MUNC18-1/DYNAMIN2 phospho-peptide substrate (100 μM) was added. The successive columns were diluted by 1.5 times. The phospho-peptide substrates were pre-incubated at 37°C for 5 min. Reactions were started by the addition of an appropriate amount of enzymes. The dephosphorylation of NSF/MUNC18-1/DYNAMIN2 was terminated by adding 120 μl Biomol green, and the enzymatic activities were monitored by measuring the absorbance at 620 nm. The steady-state kinetic parameters were determined from a direct fit of the data to the Michaelis-Menten equation using GraphPad Prism 5.0.

GST pull-down

To screen the candidate proteins interacting with PTP-MEG2, the GST beads were washed five times by cold binding buffer (20 mM HEPES pH7.5, 1 mM DTT, 1 mM EDTA, and 100 mM NaCl) and incubated with 5 μg purified GST-PTP-MEG2-CD-D⁴⁷⁰A protein for 2 h at 4°C. PC12 cells were transfected with FLAG-SYN1-GFP, FLAG-MUNC18-1-GFP, FLAG-MUNC18-1-Y¹⁴⁵A-GFP, FLAG-MUNC18-1-Y¹⁴⁵H-GFP, FLAG-MUNC18-1-Y¹⁴⁵E-GFP, FLAG-MUNC18-1-Y¹⁴⁵F-GFP, FLAG-MUNC18-3-GFP, FLAG-PACSIN1-GFP, FLAG-SCAMP1-GFP, FLAG-PPP3CA-GFP, FLAG-STX17-GFP, FLAG-VAMP7, FLAG-VAMP7-Y⁴⁵A, FLAG-VAMP7-Y⁴⁵C, FLAG-SYT7-GFP, FLAG-SYT11-GFP, FLAG-SNAP25-GFP, FLAG-SNAP25-Y¹⁰¹A-GFP, FLAG-DYNAMIN1-GFP, FLAG-DYNAMIN2, FLAG-DYNAMIN2-Y¹²⁵A, FLAG-DYNAMIN2-Y¹²⁵E, and FLAG-DYNAMIN2-Y¹²⁵F. After stimulation with 100 nM AngII for 5 min at 37°C, the cells were washed and then lysed in lysis buffer [20 mM HEPES pH 7.5, 100 mM NaCl, 0.5% NP-40, 5 mM iodoacetic acid, and a protease inhibitor mixture (final concentrations, 10 μg of leupeptin, 1 μg of aprotinin, 1 μg of pepstatin, 1 μg of antipain, and 20 μg of phenylmethylsulfonyl fluoride per ml), 10 mM DTT, 2 mM EDTA] on ice for 30 min, and then centrifuged at 10,800 g for 15 min at 4°C. 20 μl GST beads-PTP-MEG2-D⁴⁷⁰A protein was added into 500 μl supernatants, and the mixtures were subjected to end-to-end rotation at 4°C for 2 h. The GST beads and their binding proteins were washed five times with cold binding buffer to exclude the unspecific binding proteins.

The pull-down experiment of MUNC18-1 and SYNTAXIN1 was described similar to above description. The GST beads were washed five times by cold binding buffer (described as above). After that, 5 μ g purified GST-MUNC18-1-WT or its Y¹⁴⁵H, Y¹⁴⁵E, or Y¹⁴⁵F mutant proteins were added into 20 μ l GST agarose and incubated at for 4°C 2 h with end-to-end rotation. PC12 cells transfected with FLAG-SYNTAXIN1 were lysed in lysis buffer (described as above) and centrifuged to remove the pellets. The supernatants were added with 20 μ l GST beads/GST-fusion protein, and the mixtures were subjected to end-to-end rotation at 4°C for 2 h. The FLAG-SYNTAXIN1 was detected with FLAG antibody.

Co-IP

PC12 cells were infected with lentiviruses encoding GFP-tagged PTP-MEG2-D⁴⁷⁰A of wild type and different mutant types. After stimulation with 100 nM AngII for 5 min at 37°C, the cells were washed and then lysed in lysis buffer [20 mM HEPES pH 7.5, 100 mM NaCl, 0.5% NP-40, 5 mM iodoacetic acid, and a protease inhibitor mixture (final concentrations, 10 μ g of leupeptin, 1 μ g of aprotinin, 1 μ g of pepstatin, 1 μ g of antipain, and 20 μ g of phenylmethylsulfonyl fluoride per ml), 10 mM DTT, 2 mM EDTA] on ice for 30 min, and then centrifuged at 10,800 g for 15 min at 4°C. The GFP beads were washed five times by cold binding buffer (20 mM HEPES pH7.5, 1 mM DTT, 1 mM EDTA, and 100 mM NaCl). 25 μ l anti-GFP-antibody-conjugated beads were added into 500 μ l supernatants, and the mixtures were subjected to end-to-end rotation at 4°C for 2 h. The PTP-MEG2-D⁴⁷⁰A-GFP proteins were pulled down and washed five times with cold binding buffer to exclude the unspecific binding proteins. The associated PTP-MEG2 substrates in the GFP pull-down beads were then examined by Western blot.

Immunoprecipitation and *in vitro* dephosphorylation

Rat adrenal medullas were isolated and cut into pieces in D-hanks buffer and stimulated with 70 mM KCl or 100 nM AngII for 5 min. The tissues were then lysed and grinded on ice in lysis buffer supplemented with proteinase inhibitor as described before. The lysates were centrifuged at 10,800 g for 20 min at 4°C, and the pellets were removed. Before incubation with the lysates in the later step, the 1 μ g primary antibodies of NSF, MUNC18-1, VAMP7, SNAP25, or DYNAMIN2 were incubated with 20 μ l Protein A/G beads by end-to-end rotation overnight at 4°C. Then, the supernatants were incubated with primary antibody pre-coated with Protein A/G beads and rotated for 2 h. 5 μ g purified PTP-MEG2-WT protein or control solution was added into the lysates for the *in vitro* dephosphorylation. A pan-phospho-tyrosine antibody pY²⁰/pY⁹⁹ was used in Western blotting to detect the phosphorylated tyrosine of NSF/MUNC18-1/VAMP7/SNAP25/DYNAMIN2 in adrenal medullar with or without incubation with the PTP-MEG2.

Protein expression and purification

The wide type and mutant proteins of His-tagged PTP-MEG2-catalytic domain were expressed in BL21-DE3 Escherichia coli as previously described (Pan *et al.*, 2013). In brief, 0.4 mM isopropyl 1-thio-D-galactopyranoside (IPTG) was used to induce the expression of His-PTP-MEG2, and the bacteria lysates were centrifuged at 17,800 g

for 1 h (Thermo Fisher Scientific, 46910, US). Ni-NTA Agarose was applied to bind the His-tagged PTP-MEG2 and an imidazole gradient was used to elute the binding proteins. His-PTP-MEG2 was then purified with gel filtration chromatography to achieve at least 95% purity. The wide type and mutant proteins of GST-PTP-MEG2 and GST-MUNC18-1 were also expressed in E. coli in the presence of 0.4 mM IPTG for 16 h at 25°C. After lysis and centrifugation (17,800 g, Thermo Fisher Scientific, 46910, US), the proteins were purified by binding with GST-Sepharose for 2 h and eluted by GSH.

Crystallization and data collection

For crystallization, His-PTP-MEG2-C⁵¹⁵A/D⁴⁷⁰A protein (concentration at 15mg/ml) was mixed with NSF-pY⁸³ peptide (EVSLpYTFDK) or MUNC18-1-pY¹⁴⁵ peptide (ESQVpYSLDS) with molar ratio as 1:3 in buffer A (pH 7.2, 20 mM HEPES, 350 mM NaCl, and 1 mM DTT). 1 μ l mixed protein was blended with 1 μ l buffer B (pH 6.4, 20% PEG 4000, 0.2 M KSCN, 10% ethylene glycol, 0.1 M bis-tris propane) at 4°C for 3 days before crystals appear. The cubic crystals were preserved in liquid nitrogen very quickly dipped in storage buffer (buffer B supplemented with 10% glycerol). The data were collected at Shanghai Synchrotron Radiation Facility beamline BL17U1 using 0.98 Å X-ray wavelength and analyzed by HKL2000.

Structural determination and refinement

The crystals of PTP-MEG2-NSF-pY⁸³ and PTP-MEG2-MUNC18-1-pY¹⁴⁵ peptides belong to the P2₁2₁2 space group. In each asymmetric unit, both PTPMEG2-NSF-pY⁸³ and PTPMEG2-MUNC18-1-pY¹⁴⁵ contain one monomer in one unit. Molecular replacement of the MEG2-peptide complex was performed with Phaser in the CCP4 software package, with PTP-MEG2 catalytic domain (PDB code: 2PA5, water deleted) as the initial search model. Further refinements were carried out using the PHENIX program with iterative manual building in COOT. The data of the final refined structures are shown in Table 1.

BRET assay

The BRET experiment was performed to monitor the mutation effects of DYNAMIN2 on AT1aR endocytosis in response to AngII (1 μ M) stimulation as previously described (Teschemacher & Seward, 2000; Liu *et al.*, 2017). Plasmids encoding DYNAMIN2 (DYNAMIN2-WT, DYNAMIN2-Y¹²⁵E, or DYNAMIN2-Y¹²⁵F) and LYN-YFP, AT1aR-CRLUC were co-transferred into HEK293 cells at 1:1:1 ratio for 48 h. After 12 h of starvation, cells were digested with trypsin and harvested. Then, the transfected cells were washed with PBS at least three times and evenly distributed into a 96-well plate (Corning Costar Cat. # 3912). Cells were stimulated with AngII (1 μ M) for 25 min at 37°C. Afterward, coelenterazine h was incubated with the cells at 25°C (Promega S2011, final concentration, 5 μ M). We used two different light emissions for BRET measurements (530/20 nm for yellow fluorescent protein and 480/20 nm for luciferase).

GTPase activity of DYNAMIN2

To prepare His-tagged DYNAMIN2-WT, DYNAMIN2-Y¹²⁵E, and DYNAMIN2-Y¹²⁵F (His-DYNAMIN2-WT, His-DYNAMIN2-Y¹²⁵E, and

His-DYNAMIN2-Y¹²⁵F), DNA fragments were generated by PCR using MYC-DYNAMIN2 as the template and subcloned into pET-28a (+) plasmid. The resulting plasmids were transformed into bacterial BL21-DE3-RIPL cells for protein expression. The DYNAMIN proteins were then purified by affinity chromatography. We measured the DYNAMIN2 GTPase activity by using GTPase-Glo assay test kit (V7681) from Promega Corporation according to its instructions.

Bioinformatic search of PTP–protein interactions

We identified the PTP–protein interactions by two independent bioinformatic analyses. On one site, we extracted the potential PTP-interacting proteins from the STRING database (Szklarczyk *et al*, 2015) by setting the parameters of Homo sapiens. On the other site, we used PubTator (Wei *et al*, 2013) to text-mine potential PTP–protein associations from PubMed literature (by 2018.9) via the search of combinational keywords such as “tyrosine phosphorylation mutation, vesicular, fusion, and human”. We compared these two protein lists to produce a consensus PTP-interacting protein list. Subsequently, we narrowed down the protein list by satisfying following constraints: (i) The protein should express in the adrenal gland as documented in the TissueAtlas (Thul *et al*, 2017); (ii) the protein should expose tyrosine residue(s) on surface for phosphorylation as simulated by the Molecular Operating Environment (MOE; Vilar *et al*, 2008); and (iii) on the protein, at least one predicted tyrosine phosphorylation site predicted by the PhosphoSitePlus (Hornbeck *et al*, 2015) is also experiment-validated. The refined PTP–protein pairs were then ready for later experimental analyses.

LC-MS/MS analysis

Rat adrenal medullas were isolated and cut into pieces in D-hanks buffer and stimulated with 100 nM AngII for 5 min. The tissues were then lysed and grinded on ice in lysis buffer supplemented with protease inhibitors. The lysates were centrifuged at 10,800 g for 20 min at 4°C, and the pellets were removed. Before incubation with the lysates in the later step, the GST beads were washed five times by cold binding buffer (20 mM HEPES pH7.5, 1 mM DTT, 1 mM EDTA, and 100 mM NaCl) and incubated with 5 µg purified GST-PTP-MEG2-CD-D⁴⁷⁰A protein for 2 h at 4°C. 20 µl GST beads-PTP-MEG2-D⁴⁷⁰A protein was added into 500 µl supernatants, and the mixtures were subjected to end-to-end rotation at 4°C for 2 h. The GST beads and their binding proteins were washed five times with cold binding buffer to exclude the unspecific binding proteins. Denatured proteins were separated by 10% SDS–PAGE and subjected to trypsin digestion. Phosphopeptides were analyzed by the LTQ Orbitrap Elite (Thermo Scientific, Beijing Qinglian Biotech Co., Ltd). Spectra were analyzed by Proteome Discoverer software, and phosphorylation sites were confirmed manually.

Protein degradation assay

HEK293 cells were seeded in 6-well plates. Plasmids encoding MUNC18-1 (MUNC18-1-WT, MUNC18-1-Y¹⁴⁵E, or MUNC18-1-Y¹⁴⁵F) or DYNAMIN2 (DYNAMIN2-WT, DYNAMIN2-Y¹²⁵E, or DYNAMIN2-Y¹²⁵F) were transferred into HEK293 cells for 24 h. Cells were treated with cycloheximide (CHX 10µg/ml) and harvested at different time points (0, 4, 8, 12 h) for Western blot analysis.

Statistical analysis

All data are presented as mean ± s.e.m. All data were analyzed using two-tailed Student's t-test or one-way ANOVA. All Western films were scanned, and band intensity was quantified with ImageJ software (National Institutes of Health, Bethesda MD). $P < 0.05$ was considered as statistically significant.

Data availability

The coordinates and density map for the PTP-MEG2-NSF-pY⁸³ (PDB ID: 6KZQ, <http://www1.rcsb.org/structure/6KZQ>) and PTP-MEG2-MUNC18-1-pY¹⁴⁵ (PDB ID: 6L03, <http://www1.rcsb.org/structure/6L03>) peptides have been deposited in protein data bank. All other data are available upon request to the corresponding authors.

Expanded View for this article is available online.

Acknowledgements

We thank Dr Michael Xi Zhu for stimulating discussions and critical reading of the manuscript. We thank Yanmei Lu from Shandong jiaotong hospital, for her help with transmission electron microscopy analysis. We thank Daolai Zhang and Mingliang Ma for their technical assistance in lentivirus packaging. We thank Yujing Sun and Zhixin Liu for their technical assistance in electrochemical recording. We acknowledge support from the National Key Basic Research Program of China Grant 2018YFC1003600 (to X.Y. and J.-P.S.), the National Natural Science Foundation of China Grant 81773704 (to J.-P.S.), Grant 31701230 (to Z.Y.), Grant 81700473 (to C.-H.L.), and Grant 82072676 (to Y.-F.X.), the Shandong Provincial Natural Science Foundation, China (ZR2017BC045 to Z.Y.), the Fundamental Research Funds of Shandong University (2017JQ02 to J.-P.S.), the COVID-19 Emergency Tackling Research Program of Shandong University (2020XGB02 to J.-P.S.), Academic Promotion Programme of Shandong First Medical University (2019QL009 to C.-H.L.), the China Postdoctoral Science Foundation Grant 2020M682190 (to Y.-F X), the Major Fundamental Research Program of the Natural Science Foundation of Shandong Province, China (ZR2020ZD39 to J.-P.S.), the Key Research Project of the Natural Science Foundation of Beijing, China (Z200019 to J.-P.S.), the National Science Fund for Distinguished Young Scholars Grant 81825022 (to J.-P.S.), the National Science Fund for Excellent Young Scholars Grant 81822008 (to X.Y.), and the Shandong University Multidisciplinary Research and Innovation Team of Young Scholars 2020QNQT002 (to Y.-F.X.); S.Z. and Z.-Y. Z. are supported by NIH RO1 CA69202.

Author contributions

J-PS and XY conceived the whole research and initiated the project. J-PS, XY, Y-FX, and MC designed all the experiments. J-PS and XY supervised the overall project design and execution. XC, Y-FX, ZY, MC, XY, and J-PS participated in data analysis and interpretation. C-HL and Y-JW performed electrochemical experiments. ZY, PX, and Z-LZ helped us collect crystal data and analyze crystal structure. MC, K-SL, and Y-CS performed cell biology, molecular biology, and biochemistry experiments. Z-GX provided DYNAMIN2 plasmid. Z-YZ and SZ synthesized and purified Compound 7 (PTP-MEG2 inhibitor). X-ZY and Z-LJ performed substrate bioinformatics screening. Z-YZ, W-DZ, C-HW, and CW provided insightful idea and experimental designs. J-PS, Y-FX, XC, and XY wrote the manuscript. All of the authors have seen and commented on the manuscript.

Conflict of interest

The authors declare that they have no conflict of Interest.

References

- Alonso A, Sasin J, Bottini N, Friedberg I, Osterman A, Godzik A, Hunter T, Dixon J, Mustelin T (2004) Protein tyrosine phosphatases in the human genome. *Cell* 117: 699–711
- Alvarez de Toledo G, Fernandez-Chacon R, Fernandez JM (1993) Release of secretory products during transient vesicle fusion. *Nature* 363: 554–558
- Baker RW, Hughson FM (2016) Chaperoning SNARE assembly and disassembly. *Nat Rev Mol Cell Biol* 17: 465–479
- Ballif BA, Carey GR, Sunyaev SR, Gygi SP (2008) Large-scale identification and evolution indexing of tyrosine phosphorylation sites from murine brain. *J Proteome Res* 7: 311–318
- Barr AJ, Ugochukwu E, Lee WH, King ON, Filippakopoulos P, Alfano I, Savitsky P, Burgess-Brown NA, Muller S, Knapp S (2009) Large-scale structural analysis of the classical human protein tyrosine phosphatome. *Cell* 136: 352–363
- Chai YJ, Sierrecki E, Tomatis VM, Gormal RS, Giles N, Morrow IC, Xia D, Gotz J, Parton RG, Collins BM et al (2016) Munc18-1 is a molecular chaperone for alpha-synuclein, controlling its self-replicating aggregation. *J Cell Biol* 214: 705–718
- Chen XK, Wang LC, Zhou Y, Cai Q, Prakriya M, Duan KL, Sheng ZH, Lingle C, Zhou Z (2005) Activation of GPCRs modulates quantal size in chromaffin cells through G(betagamma) and PKC. *Nat Neurosci* 8: 1160–1168
- Cho CY, Koo SH, Wang Y, Callaway S, Hedrick S, Mak PA, Orth AP, Peters EC, Saez E, Montminy M et al (2006) Identification of the tyrosine phosphatase PTP-MEG2 as an antagonist of hepatic insulin signaling. *Cell Metab* 3: 367–378
- Cijsouw T, Weber JP, Broeke JH, Broek JA, Schut D, Kroon T, Saarloos I, Verhage M, Toonen RF (2014) Munc18-1 redistributes in nerve terminals in an activity- and PKC-dependent manner. *J Cell Biol* 204: 759–775
- Dittman JS, Ryan TA (2019) The control of release probability at nerve terminals. *Nat Rev Neurosci* 20: 177–186
- Doody KM, Bottini N (2014) "PEST control": regulation of molecular barcodes by tyrosine phosphatases. *Cell Res* 24: 1027–1028
- Eitzen G (2003) Actin remodeling to facilitate membrane fusion. *Biochem Biophys Acta* 1641: 175–181
- Fisher RJ, Pevsner J, Burgoyne RD (2001) Control of fusion pore dynamics during exocytosis by Munc18. *Science* 291: 875–878
- Frijhoff J, Dagnell M, Godfrey R, Ostman A (2014) Regulation of protein tyrosine phosphatase oxidation in cell adhesion and migration. *Antioxid Redox Signal* 20: 1994–2010
- Gabel M, Delavoie F, Royer C, Tahouly T, Gasman S, Bader MF, Vitale N, Chasserot-Golaz S (2019) Phosphorylation cycling of Annexin A2 Tyr23 is critical for calcium-regulated exocytosis in neuroendocrine cells. *Biochim Biophys Acta* 1866: 1207–1217
- Gaisano HY (2017) Recent new insights into the role of SNARE and associated proteins in insulin granule exocytosis. *Diabetes Obes Metab* 19 (Suppl 1): 115–123
- Gu M, Warshawsky I, Majerus PW (1992) Cloning and expression of a cytosolic megakaryocyte protein-tyrosine-phosphatase with sequence homology to retinaldehyde-binding protein and yeast SEC14p. *Proc Natl Acad Sci USA* 89: 2980–2984
- Gulyas-Kovacs A, de Wit H, Milosevic I, Kochubey O, Toonen R, Klingauf J, Verhage M, Sorensen JB (2007) Munc18-1: sequential interactions with the fusion machinery stimulate vesicle docking and priming. *J Neurosci* 27: 8676–8686
- Harada K, Matsuoka H, Miyata H, Matsui M, Inoue M (2015) Identification of muscarinic receptor subtypes involved in catecholamine secretion in adrenal medullary chromaffin cells by genetic deletion. *Br J Pharmacol* 172: 1348–1359
- He E, Wierda K, van Westen R, Broeke JH, Toonen RF, Cornelisse LN, Verhage M (2017) Munc13-1 and Munc18-1 together prevent NSF-dependent de-priming of synaptic vesicles. *Nat Commun* 8: 15915
- Hernandez JM, Stein A, Behrmann E, Riedel D, Cypionka A, Farsi Z, Walla PJ, Raunser S, Jahn R (2012) Membrane fusion intermediates via directional and full assembly of the SNARE complex. *Science* 336: 1581–1584
- Hong W, Lev S (2014) Tethering the assembly of SNARE complexes. *Trends Cell Biol* 24: 35–43
- Hornbeck PV, Zhang B, Murray B, Kornhauser JM, Latham V, Skrzypek E (2015) PhosphoSitePlus, 2014: mutations, PTMs and recalibrations. *Nucleic Acids Res* 43: D512–D520
- Hu SH, Christie MP, Saez NJ, Latham CF, Jarrott R, Lua LH, Collins BM, Martin JL (2011) Possible roles for Munc18-1 domain 3a and Syntaxin1 N-peptide and C-terminal anchor in SNARE complex formation. *Proc Natl Acad Sci USA* 108: 1040–1045
- Huynh H, Bottini N, Williams S, Cherepanov V, Musumeci L, Saito K, Bruckner S, Vachon E, Wang X, Kruger J et al (2004) Control of vesicle fusion by a tyrosine phosphatase. *Nat Cell Biol* 6: 831–839
- Jewell JL, Oh E, Ramalingam L, Kalwat MA, Tagliabracchi VS, Tackett L, Elmendorf JS, Thurmond DC (2011) Munc18c phosphorylation by the insulin receptor links cell signaling directly to SNARE exocytosis. *J Cell Biol* 193: 185–199
- Jones DM, Alvarez LA, Nolan R, Ferriz M, Sainz Urruela R, Massana-Munoz X, Novak-Kotzer H, Dustin ML, Padilla-Parra S (2017) Dynamin-2 stabilizes the HIV-1 fusion pore with a low oligomeric state. *Cell Rep* 18: 443–453
- Kanda M, Ihara Y, Murata H, Urata Y, Kono T, Yodoi J, Seto S, Yano K, Kondo T (2006) Glutaredoxin modulates platelet-derived growth factor-dependent cell signaling by regulating the redox status of low molecular weight protein-tyrosine phosphatase. *J Biol Chem* 281: 28518–28528
- Kar UP, Dey H, Rahaman A (2017) Regulation of dynamin family proteins by post-translational modifications. *J Biosci* 42: 333–344
- Korteweg N, Maia AS, Thompson B, Roubos EW, Burbach JP, Verhage M (2005) The role of Munc18-1 in docking and exocytosis of peptide hormone vesicles in the anterior pituitary. *Biol Cell* 97: 445–455
- Laidlaw KME, Livingstone R, Al-Tobi M, Bryant NJ, Gould GW (2017) SNARE phosphorylation: a control mechanism for insulin-stimulated glucose transport and other regulated exocytic events. *Biochem Soc Trans* 45: 1271–1277
- Li H, Yang F, Liu C, Xiao P, Xu Y, Liang Z, Liu C, Wang H, Wang W, Zheng W et al (2016) Crystal structure and substrate specificity of PTPN12. *Cell Rep* 15: 1345–1358
- Lim SH, Moon J, Lee M, Lee JR (2013) PTPRT regulates the interaction of Syntaxin-binding protein 1 with Syntaxin 1 through dephosphorylation of specific tyrosine residue. *Biochem Biophys Res Comm* 439: 40–46
- Liu CH, Gong Z, Liang ZL, Liu ZX, Yang F, Sun YJ, Ma ML, Wang YJ, Ji CR, Wang YH et al (2017) Arrestin-biased AT1R agonism induces acute catecholamine secretion through TRPC3 coupling. *Nat Commun* 8: 14335
- Ma C, Su L, Seven AB, Xu Y, Rizo J (2013) Reconstitution of the vital functions of Munc18 and Munc13 in neurotransmitter release. *Science* 339: 421–425
- Ma L, Rebane AA, Yang G, Xi Z, Kang Y, Gao Y, Zhang Y (2015) Munc18-1-regulated stage-wise SNARE assembly underlying synaptic exocytosis. *Elife* 4: e09580
- Magadmi R, Meszaros J, Damanhoury ZA, Seward EP (2019) Secretion of mast cell inflammatory mediators is enhanced by CADM1-dependent adhesion to sensory neurons. *Front Cell Neurosci* 13: 262

- Mallozzi C, D'Amore C, Camerini S, Macchia G, Crescenzi M, Petrucci TC, Di Stasi AM (2013) Phosphorylation and nitration of tyrosine residues affect functional properties of Synaptophysin and Dynamin I, two proteins involved in exo-endocytosis of synaptic vesicles. *Biochem Biophys Acta* 1833: 110–121
- Mattila JP, Shnyrova AV, Sundborger AC, Hortelano ER, Fuhrmans M, Neumann S, Muller M, Hinshaw JE, Schmid SL, Frolov VA (2015) A hemifission intermediate links two mechanistically distinct stages of membrane fission. *Nature* 524: 109–113
- Meijer M, Dorr B, Lammertse HC, Blithikioti C, van Weering JR, Toonen RF, Sollner TH, Verhage M (2018) Tyrosine phosphorylation of Munc18-1 inhibits synaptic transmission by preventing SNARE assembly. *EMBO J* 37: 300–320
- Neher E, Brose N (2018) Dynamically primed synaptic vesicle states: key to understand synaptic short-term plasticity. *Neuron* 100: 1283–1291
- Oakie A, Wang R (2018) beta-cell receptor tyrosine kinases in controlling insulin secretion and exocytotic machinery: c-kit and insulin receptor. *Endocrinology* 159: 3813–3821
- Ortsater H, Grankvist N, Honkanen RE, Sjöholm A (2014) Protein phosphatases in pancreatic islets. *J Endocrinol* 221: R121–144
- Pan C, Liu HD, Gong Z, Yu X, Hou XB, Xie DD, Zhu XB, Li HW, Tang JY, Xu YF et al (2013) Cadmium is a potent inhibitor of PPM phosphatases and targets the M1 binding site. *Sci Rep* 3: 2333
- Seino S, Takahashi H, Fujimoto W, Shibasaki T (2009) Roles of cAMP signalling in insulin granule exocytosis. *Diabetes Obes Metab* 11(Suppl 4): 180–188
- Shin W, Ge L, Arpino G, Villarreal SA, Hamid E, Liu H, Zhao WD, Wen PJ, Chiang HC, Wu LG (2018) Visualization of membrane pore in live cells reveals a dynamic-pore theory governing fusion and endocytosis. *Cell* 173: 934–945.e12
- Sitarska E, Xu J, Park S, Liu X, Quade B, Stepien K, Sugita K, Brautigam CA, Sugita S, Rizo J (2017) Autoinhibition of Munc18-1 modulates synaptobrevin binding and helps to enable Munc13-dependent regulation of membrane fusion. *Elife* 6: e24278
- Soares H, Henriques R, Sachse M, Ventimiglia L, Alonso MA, Zimmer C, Thoulouze MI, Alcover A (2013) Regulated vesicle fusion generates signaling nanoterritories that control T cell activation at the immunological synapse. *J Exp Med* 210: 2415–2433
- Stamberger H, Weckhuysen S, De Jonghe P (2017) STXBP1 as a therapeutic target for epileptic encephalopathy. *Expert Opin Ther Targets* 21: 1027–1036
- Sudhof TC (2004) The synaptic vesicle cycle. *Annu Rev Neurosci* 27: 509–547
- Sudhof TC (2013) Neurotransmitter release: the last millisecond in the life of a synaptic vesicle. *Neuron* 80: 675–690
- Sudhof TC, Rothman JE (2009) Membrane fusion: grappling with SNARE and SM proteins. *Science* 323: 474–477
- Szklarczyk D, Franceschini A, Wyder S, Forslund K, Heller D, Huerta-Cepas J, Simonovic M, Roth A, Santos A, Tsafou KP et al (2015) STRING v10: protein-protein interaction networks, integrated over the tree of life. *Nucleic Acids Res* 43: D447–452
- Teschemacher AG, Seward EP (2000) Bidirectional modulation of exocytosis by angiotensin II involves multiple G-protein-regulated transduction pathways in chromaffin cells. *J Neurosci* 20: 4776–4785
- Thul PJ, Akesson L, Wiking M, Mahdessian D, Geladaki A, Ait Blal H, Alm T, Asplund A, Bjork L, Breckels LM et al (2017) A subcellular map of the human proteome. *Science* 356: eaal3321
- Tonks NK (2006) Protein tyrosine phosphatases: from genes, to function, to disease. *Nat Rev Mol Cell Biol* 7: 833–846
- Umahara M, Okada S, Yamada E, Saito T, Ohshima K, Hashimoto K, Yamada M, Shimizu H, Pessin JE, Mori M (2008) Tyrosine phosphorylation of Munc18c regulates platelet-derived growth factor-stimulated glucose transporter 4 translocation in 3T3L1 adipocytes. *Endocrinology* 149: 40–49
- Vilar S, Cozza G, Moro S (2008) Medicinal chemistry and the molecular operating environment (MOE): application of QSAR and molecular docking to drug discovery. *Curr Top Med Chem* 8: 1555–1572
- Wang HM, Xu YF, Ning SL, Yang DX, Li Y, Du YJ, Yang F, Zhang Y, Liang N, Yao W et al (2014) The catalytic region and PEST domain of PTPN18 distinctly regulate the HER2 phosphorylation and ubiquitination barcodes. *Cell Res* 24: 1067–1090
- Wang Y, Vachon E, Zhang J, Cherepanov V, Kruger J, Li J, Saito K, Shannon P, Bottini N, Huynh H et al (2005) Tyrosine phosphatase MEG2 modulates murine development and platelet and lymphocyte activation through secretory vesicle function. *J Exp Med* 202: 1587–1597
- Wei CH, Kao HY, Lu Z (2013) PubTator: a web-based text mining tool for assisting biocuration. *Nucleic Acids Res* 41: W518–522
- Wu LG, Hamid E, Shin W, Chiang HC (2014) Exocytosis and endocytosis: modes, functions, and coupling mechanisms. *Annu Rev Physiol* 76: 301–331
- Yang X, Wang S, Sheng Y, Zhang M, Zou W, Wu L, Kang L, Rizo J, Zhang R, Xu T et al (2015) Syntaxin opening by the MUN domain underlies the function of Munc13 in synaptic-vesicle priming. *Nat Struct Mol Biol* 22: 547–554
- Yu X, Chen M, Zhang S, Yu ZH, Sun JP, Wang L, Liu S, Imasaki T, Takagi Y, Zhang ZY (2011) Substrate specificity of lymphoid-specific tyrosine phosphatase (Lyp) and identification of Src kinase-associated protein of 55 kDa homolog (SKAP-HOM) as a Lyp substrate. *J Biol Chem* 286: 30526–30534
- Yu ZH, Zhang ZY (2018) Regulatory mechanisms and novel therapeutic targeting strategies for protein tyrosine phosphatases. *Chem Rev* 118: 1069–1091
- Zhang D, Marlin MC, Liang Z, Ahmad M, Ashpole NM, Sonntag WE, Zhao ZJ, Li G (2016) The protein tyrosine phosphatase MEG2 regulates the transport and signal transduction of tropomyosin receptor kinase A. *J Biol Chem* 291: 23895–23905
- Zhang DL, Sun YJ, Ma ML, Wang YJ, Lin H, Li RR, Liang ZL, Gao Y, Yang Z, He DF et al (2018) Gq activity- and beta-arrestin-1 scaffolding-mediated ADGRG2/CFTR coupling are required for male fertility. *Elife* 7: e33432
- Zhang S, Liu S, Tao R, Wei D, Chen L, Shen W, Yu ZH, Wang L, Jones DR, Dong XC et al (2012) A highly selective and potent PTP-MEG2 inhibitor with therapeutic potential for type 2 diabetes. *J Am Chem Soc* 134: 18116–18124
- Zhao WD, Hamid E, Shin W, Wen PJ, Krystofiak ES, Villarreal SA, Chiang HC, Kachar B, Wu LG (2016) Hemi-fused structure mediates and controls fusion and fission in live cells. *Nature* 534: 548–552
- Zhou Z, Mislis S, Chow RH (1996) Rapid fluctuations in transmitter release from single vesicles in bovine adrenal chromaffin cells. *Biophys J* 70: 1543–1552